Journal of Nanobiotechnology

RESEARCH

Open Access

Rationally designed NIR-II excitable and endoplasmic reticulum-targeted molecular phototheranostics for imaging-guided enhanced photoimmunotherapy of triple-negative breast cancer

Fen Liu[1,2†], Qiang Kang[1†], Hao Xiao[1], Yinying Liu[1], Sengyou Tan[1], Kun Fan[2], Jianchun Peng[2], Xiaofeng Tan[1,3*], Guilong Wu[1,3*] and Qinglai Yang[1,3*]

Abstract

Triple-negative breast cancer (TNBC) is a highly aggressive subtype of breast cancer characterized by an extremely poor prognosis. Photoimmunotherapy has emerged as a promising strategy for the treatment of TNBC. This approach works by selectively destroying tumor cells, releasing tumor-associated antigens, activating the immune system, and effectively inhibiting tumor proliferation and metastasis. However, the majority of current phototheranostic approaches are hindered by limited tissue penetration in the first near-infrared (NIR-I) and ultraviolet–visible (UV–Vis) regions. Additionally, due to the lack of specific subcellular targets, it may be difficult to effectively treat deep-seated lesions with ambiguous and extensive boundaries caused by TNBC metastases. Consequently, the development of effective, deep-penetrating, organelle-targeted phototheranostics is essential for enhancing treatment outcomes in TNBC. This work proposes a novel molecular design strategy of NIR-II phototheranostics to realize planar rigid conjugation and alkyl chain functionalization. The di-hexaalkyl chains in a vertical configuration on the donor (4H-cyclopenta[2,1-b:3,4-b'] dithiophene) and shielding units (fluorene) are introduced to construct a S-D-A-D-S type NIR-II phototheranostics (IR-FCD). The planar and rigid structure of IR-FCD exhibits a robust intramolecular charge transfer capability, a lower band gap, enhanced photon absorption properties, and significant steric hindrance from vertically arranged alkyl chains to minimize non-radiative energy loss. By incorporating N-(but-3-yn-1-yl)-4-methylbenzenesulfonamide at the terminus of an elongated alkyl chain, followed by self-assembly into DSPE-S-S-PEG2000, NIR-II excitable phototheranostics (IR-FCD-Ts NPs) with endoplasmic reticulum (ER) targeting capability were successfully synthesized for imaging-guided photoimmunotherapy of TNBC. The IR-FCD-Ts NPs demonstrate exceptional optical characteristics, with maximum absorption at 1068 nm (extending to 1300 nm) and emission at 1273 nm (extending to 1700 nm), along with a high molar absorption coefficient of $2.76*10^4$ L/mol·c at 1064 nm

†Fen Liu and Qiang Kang have contributed equally to this work.

*Correspondence:
Xiaofeng Tan
tanxiaofeng@usc.edu.cn
Guilong Wu
2018000014@usc.edu.cn
Qinglai Yang
qingyu513@usc.edu.cn
Full list of author information is available at the end of the article

in aqueous solution. Under exposure to 1064 nm laser irradiation, IR-FCD-Ts NPs exhibit superior photothermal properties and have the potential for photodynamic therapy. By targeting ER, thereby inducing ER stress and significantly enhancing immunogenic cell death (ICD) in tumor cells, it triggers a strong antitumor immune response and inhibits the proliferation and metastasis of TNBC.

Keywords NIR-II, Phototheranostics, Endoplasmic reticulum, Triple-negative breast cancer, Intermolecular π–π stacking interaction

Graphical Abstract

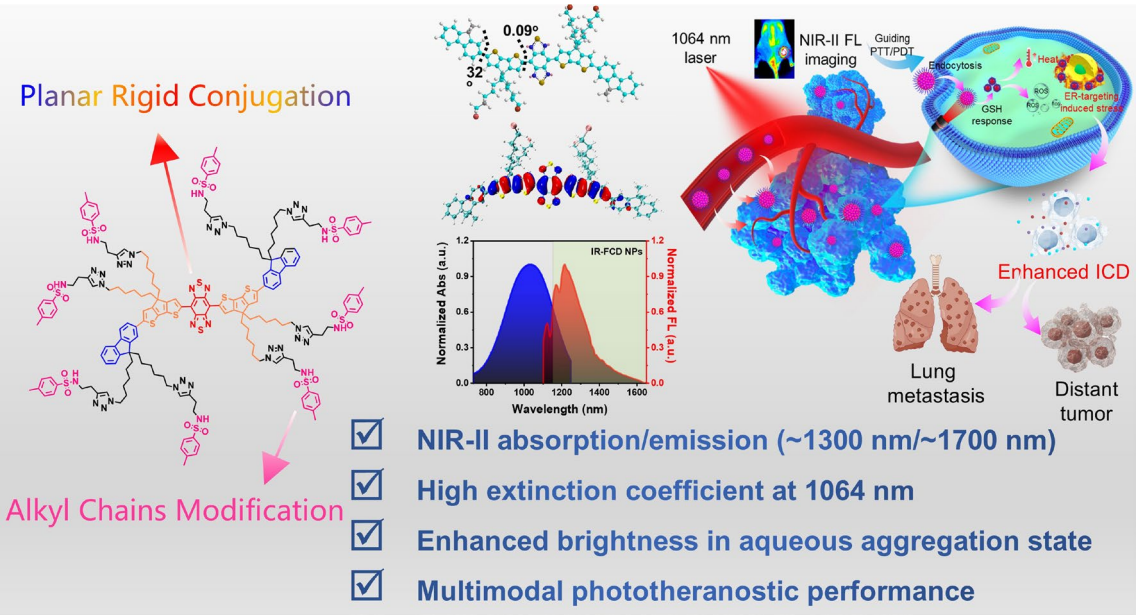

Background

Breast cancer remains the most prevalent malignant neoplasm worldwide, with the highest incidence and mortality rates in women. Among its subtypes, triple-negative breast cancer (TNBC) poses the greatest threat due to its pronounced invasiveness and metastatic potential, causing high recurrence rates and unfavorable prognostic outcomes [1, 2]. Despite notable advancements in clinical treatment modalities for TNBC, including surgery, chemotherapy, and radiotherapy, substantial challenges remain, particularly regarding drug resistance and adverse effects [3, 4]. It is indisputable that effective and safe innovative therapeutic strategies for TNBC are urgently needed.

Phototheranostic has offered a novel perspective for high-resolution imaging diagnosis and accurate phototherapy of the tumor by the necrosis and apoptosis pathways with minimal invasiveness, high spatiotemporal controllability, and low toxicity [5]. Intriguingly, phototherapy is considered to have substantial potential in initiating immunogenic cell death (ICD), resulting in the release of tumor-associated antigens (TAAs) and damage-associated molecular patterns (DAMPs) such as surface-exposed calreticulin (CRT), passively released high-mobility group box1 (HMGB1), and secreted adenosine triphosphate (ATP). The release of DAMPs stimulates the host immune system by promoting the maturation of dendritic cells (DCs) and the differentiation of cytotoxic T-lymphocytes (CTLs). Additionally, the secreted cytokines by the immunologic process, such as interferon-γ (IFN-γ), tumor necrosis factor-α (TNF-α), and various interleukins (IL), also play a significant role in contributing to immunotherapy [6, 7]. However, conventional phototheranostics are hindered by limited tissue penetration in the first near-infrared (NIR-I) and ultraviolet–visible (UV–Vis) regions. Additionally, due to the lack of specific subcellular targets, as well as the immunosuppressive microenvironment of TNBC [8, 9]. It may be difficult to effectively treat deep-seated lesions with

ambiguous and extensive boundaries caused by TNBC metastases.

The deep tissue penetration and maximum permissible exposure (MPE) of the second near-infrared (NIR-II, 1000–1700 nm) phototheranostic technology propose an innovative and efficacious remedy for the diagnosis and treatment of TNBC [10, 11]. The key factor in harnessing the advantages of NIR-II phototheranostic technology is selecting all-round phototheranostics, which requires a combination of various optical properties (fluorescence, photoacoustic, photothermal, photodynamic, etc.) and good biocompatibility [12, 13]. The molecular phototheranostics with NIR-II absorbing wavelength (> 1000 nm) possess lower photo scattering and reabsorption. Moreover, compared to inorganic and polymeric materials, they exhibit significant advantages such as controllable optical properties, adjustable targeting modifications, and superior clearance effects [13–15]. Nevertheless, the intricate photophysical processes pose a considerable challenge for enabling multimodal NIR-II molecular phototheranostics that simultaneously achieve fluorescence (radiative transition), photothermal (non-radiative transition), and photodynamic properties (reactive oxygen species (ROS) generation by the triplet state) [16, 17]. At present, the common molecular phototheranostics with NIR-II absorption, such as cyanine, boron dipyrromethene (BODIPY), and squaraine derivatives, have been extensively developed for a variety of commercial applications. However, several drawbacks, including aqueous environment-enhanced aggregation-caused quenching (ACQ), small stokes shift (< 100 nm), and unstable intramolecular double bonds, hamper their practical applications [18–20].

The emerging donor–acceptor-donor (D-A-D) structured conjugated molecules with NIR-II absorption are attracting substantial interest due to their excellent biocompatibility, structural modifiability, and tunable optical properties. Ling and colleagues successfully synthesized a CSM2 molecule with NIR-II absorption by incorporating thiophene to extend the conjugation structure for enabling NIR-II PAI-guided PTT for tumor eradication [17]. Liu et al. leverage the enhanced donor–acceptor (D-A) electron push–pull strategy by incorporating a boron difluoride group into the conjugated molecule, thereby achieving NIR-II absorption and superior photothermal performance [21, 22]. In the aforementioned molecular designs, the photothermal performances from non-radiative transition energy are primarily enhanced by the reduction in the band gap, which yet compromises their NIR-II fluorescence performance. Therefore, Fan et al. strengthened the molecular planarity by introducing the donor group with significant steric hindrance and alkyl chain modification to collectively improve NIR-II fluorescence imaging and photothermal performances. However, the restricted donor–acceptor electron push–pull capability only led to the trailing of the absorption band at 1064 nm [23, 24]. Similarly, Wang et al. constructed a strongly conjugated and electron-donating extended structure by utilizing tetrastyrene/triphenylamine and 4,7-dihydrobenzo[c]thiophene/3,4-Ethylenedioxy-thiophene (EDOT) for simultaneously achieving excellent NIR-II absorption and emission. The distorted molecular structure can mitigate the ACQ effect while reducing the maximum absorption wavelength and attenuating the photon absorption to some extent [25, 26]. Concurrently, the excited state (S_1) of the D-A-D conjugated molecules is predominantly influenced by polar water molecules (H_2O) to diminish gap crossing ability, impeding the transition from the excited state (S_1) to the excited triplet state (T_1) [27]. Therefore, the substantial challenge remains in regulating the D-A-D molecules to realize the balance of NIR-II absorption, fluorescence, photothermal, and photodynamic properties.

Meanwhile, organelle-targeting strategy is extensively reported to enhance tumor phototherapy effectiveness [22, 23, 28]. The endoplasmic reticulum (ER) is critical for protein synthesis, folding, and post-translational modification in cells [29]. Various factors, such as hyperthermia and ROS, can disrupt the protein folding process within the ER, leading to ER stress and subsequently triggering ICD [30]. Previous studies [31–35] have demonstrated that ER-targeted phototheranostics can amplify ICD by inducing ER stress. Therefore, ER-targeted phototheranostics not only enhance the local cytotoxicity against tumor cells but also promote the release of tumor antigens, which in turn activates the anti-tumor immune response, thereby enhancing the anti-tumor efficacy. Nevertheless, the phototheranostics in previous studies were mainly limited to the NIR-I region. Consequently, there is a pressing need to develop NIR-II phototheranostics (especially the NIR-II excitation) with ER-targeted capabilities.

In previous research, a category of shielding-donor–acceptor-donor-shielding (S-D-A-D-S) typed NIR-II phototheranostics was developed for bioimaging-guided biotherapy [27, 36–42]. While such molecular engineering effectively enhances QY in aqueous solutions, it concurrently induces significant distortion of the conjugated backbones, leading to an undesired hypsochromic shift in both the absorption (extending to 1000 nm), emission (extending to 1400 nm), and a reduction in absorption coefficient ($\varepsilon = 0.1–1.3$ (10^4L/mol·cm). Herein, we propose a novel molecular design strategy by introducing di-hexaalkyl chains with a vertical configuration and large steric hindrance on the donor (4H-cyclopenta

[2,1-b: 3,4-b'] dithiophene) and shielding units (fluorene) to construct an S-D-A-D-S typed NIR-II phototheranostics (IR-FCD). Specifically, the use of this donor (D) demonstrates a potent electron-donating that enhances intramolecular charge transfer capability, while its bulky alkyl chain can mitigate intermolecular π–π stacking capacity. Importantly, it is ingenious that there is no steric hindrance effect between D and A, thus avoiding molecular distortion and preserving the intramolecular charge transfer efficiency. This results in the formation of a planar and rigid IR-FCD with a robust intramolecular charge transfer ability, a lower band gap, and enhanced photon absorption ability. Moreover, the large steric hindrance from the bulky alkyl chains with vertical configuration can attenuate the intermolecular π–π stacking interaction to minimize the loss of non-radiative energy. Additionally, the IR-FCD molecule could maintain strong fluorescence emission performance in the aggregation state.

According to previous studies, the side chains of this class of molecules can be efficiently functionalized and modified with improved anti-tumor efficacy [43–45]. Afterward, the N-(but-3-yn-1-yl)-4-methylbenzenesulfonamide was modified on the terminal of stretched alkyl chains to endow the IR-FCD with ER- targeted ability (IR-FCD-Ts). Ultimately, water-soluble and redox-responsive IR-FCD-Ts nanoparticles (IR-FCD NPs) were obtained through the assembly of IR-FCD-Ts molecules and disulfide bond-containing lipid-PEG (DSPE-S-S-PEG2000). The IR-FCD NPs/IR-FCD-Ts NPs exhibit excellent optical properties with maximum absorption at 1058/1068 nm (extending to 1300 nm)/emission at 1256/1273 nm (extending to 1700 nm), and a high molar absorption coefficient ($1.96*10^4$/$2.76*10^4$ L/mol·c at 1064 nm in water). Finally, IR-FCD-Ts NPs were used for NIR-II fluorescence imaging-guided photoimmunotherapy for TNBC. Encouragingly, under 1064 nm laser irradiation, IR-FCD-Ts NPs have good photothermal properties along with photodynamic therapy potential. Both in vivo and in vitro experiments demonstrated the good biocompatibility of IR-FCD-Ts NPs. Furthermore, the ER-targeted phototherapy induces a significant ICD enhancement to subsequently activate a strong antitumor immune response, thereby inhibiting not only the primary tumors growth of TNBC but also the proliferation of metastatic tumors (Scheme 1).

Results and discussion

Molecular design and theoretical calculation

As illustrated in Scheme 1, for the design of the IR-FCD molecule, dialkyl substituted fluorene and cyclopenta dithiophene are utilized as the shielding and donor unit, respectively, to reduce the intermolecular π–π stacking interactions [37, 42, 43]. The dialkyl-substituted cyclopenta-dithiophene has no steric hindrance with the acceptor (BBTD) to cause molecular distortion, thus leading to the strengthening of the intramolecular charge transfer. The rigid planar conjugated backbone of IR-FCD and strong intramolecular charge transfer capability make the molecule have a low band gap and strong photon absorption, endowing it with NIR-II optical properties of the long wavelength (absorption peak at 1056 nm and extending to 1300 nm, emission peak at 1320 nm and extending to 1700 nm), a high molar extinction coefficient (ε), and the reduced intermolecular π-stacking interactions that mean an attenuated non-radiative energy loss and an enhanced fluorescence emission in the aggregated state. To achieve a more extensive understanding of the donor engineering design of the IR-FCD (IR represents the near-infrared, F represents the fluorene, and CD represents the cyclopenta dithiophene), a comparative analysis was conducted using the IR-FTT (IR refers to near-infrared, F represents the fluorene, and TT signifies a conjugated bithiophene) [27] as a counterpart to IR-FCD.

To investigate the electronic properties and geometrical structures of the IR-FTT and IR-FCD molecular fluorophores, density functional theory (DFT) and time-dependent density functional theory (TDDFT) calculations were conducted (Supplementary Information for computational details). As presented in Fig. 1A, the frontier molecular orbitals calculation of IR-FTT and IR-FCD indicated the detailed information of the highest occupied molecular orbital (HOMO) and the lowest unoccupied molecular orbital (LOMO). The results displayed that the HOMO orbitals of two molecules were distributed along the conjugated structure while the LOMO orbitals concentrated on the BBTD unit. Moreover, the HOMO–LUMO energy band gaps of IR-FCD (calculated as 1.10 eV) are lower than that of IR-FTT (calculated as 1.27 eV). Notably, the LUMO distribution of IR-FCD is more confined to the BBTD molecule compared to IR-FTT (Table S1). The lower LUMO of IR-FCD could be attributed to the simple design of the donor component to cause fewer intermolecular interactions by the calculation results.

As shown in Fig. 1B, the optimized ground-state (S_0) geometries disclose the twisted conformations of IR-FTT and IR-FCD. The dihedral angle between the donor and acceptor for IR-FTT and IR-FCD is 2° and 0.09°, respectively (the dihedral angle between D2 and D1 for IR-FTT is 9°). The dihedral angles between the donor (D) and shielding unit (S) for IR-FTT and IR-FCD are 33° and 32°, respectively. In terms of linear torsion, IR-FCD appears to present a better planarity than IR-FTT. This result appears to indicate that IR-FCD

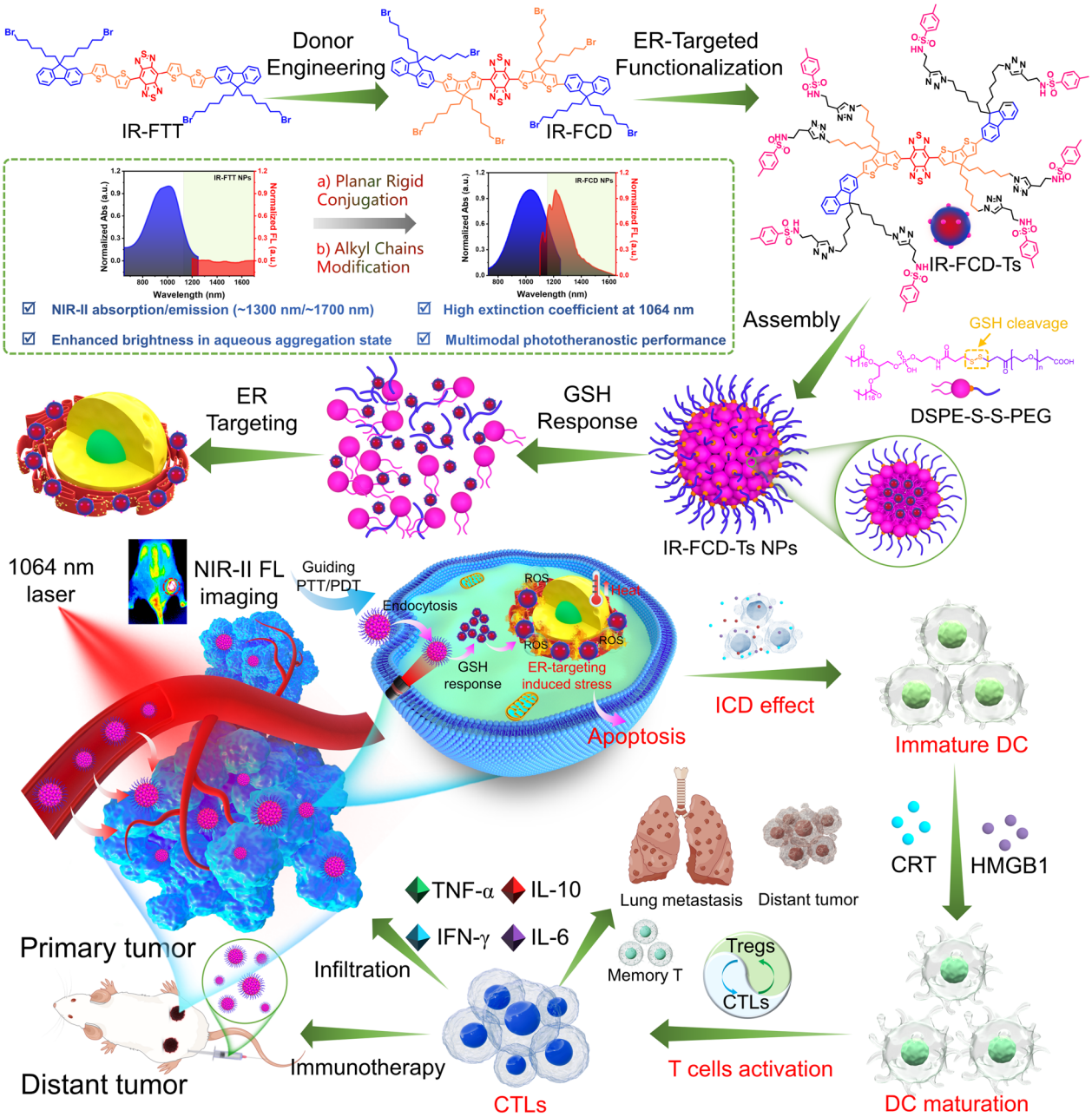

Scheme 1 NIR-II excitable molecular phototheranostics for NIR-II imaging-guided ER-targeted photoimmunotherapy for TNBC

exhibits higher intermolecular face-to-face π–π stacking interactions than IR-FTT. However, it can be found that the red-shifted wavelengths of IR-FTT NPs and IR-FCD NPs in the aqueous solution aggregation state are 120 nm and 2 nm, respectively, compared with IR-FTT and IR-FCD in the DCM dispersion state (Fig. S12), which indicates that IR-FTT has stronger intermolecular π–π stacking interactions in the aggregation state, resulting in red shifts [46, 47]. Therefore, there are other factors influencing π–π stacking interactions than linear torsion. In IR-FCD, Dialkyl substituted fluorene and cyclopenta dithiophene are utilized as the shielding and donor unit, respectively, as they have been reported to reduce the intermolecular π–π stacking interactions between their conjugate skeletons [37, 42, 43]. The above result confirmed that IR-FTT exhibits higher intermolecular π–π stacking interactions than IR-FCD.

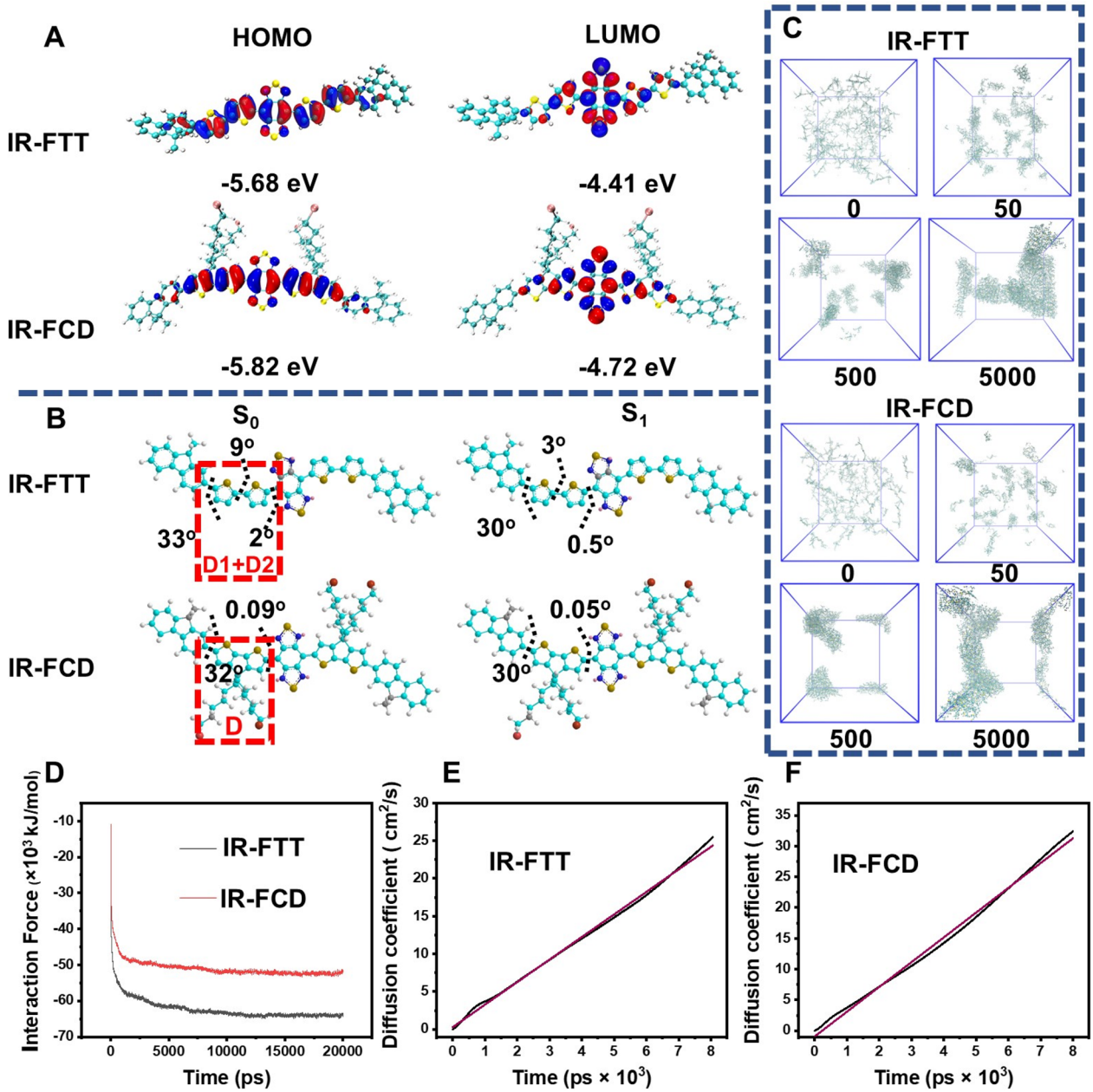

Fig. 1 **A** Calculated HOMOs and LUMOs of IR-FTT and IR-FCD. **B** Optimized ground-state (S_0) and first singlet excited state (S_1) geometries of IR-FTT and IR-FCD. **C** Molecular dynamics simulations of IR-FTT and IR-FCD. **D** Interaction force of IR-FTT and IR-FCD. Diffusion coefficient of **E** IR-FTT and **F** IR-FCD

To further explore the mechanism that the introduced dialkyl substituted cyclopenta dithiophene can reduce the intermolecular interactions of the planar and narrow band gap NIR-II fluorophore IR-FCD in the aggregated state. The designed NIR-II fluorophores were simulated by molecular dynamics (MD) to gain insight into their intermolecular interactions (100 monomers of each aggregate to mimic their behavior in real systems) (Supplementary Information for computational details). As shown in Fig. 1C, the molecular motion trajectories of IR-FTT and IR-FCD in confined spaces were observed, ranging from 0 to 5000 ps. The linear simulation results indicated that the molecular force stabilized at 64,118 kJ/mol for IR-FTT and 52,054 kJ/mol for IR-FCD (Fig. 1D). In addition, the corresponding diffusion coefficients IR-FTT and IR-FCD are 0.7824×10^{-5} and

1.0957×10^{-5} cm^2/s, respectively (Fig. 1E and Fig. 1F). The results demonstrated that the intermolecular interactions of IR-FCD were relieved compared with IR-FTT owing to the introduction of the dialkyl-substituted cyclopenta dithiophene.

Synthesis and characterization

The IR-FCD molecule was synthesized via the stille reaction, with dialkyl-substituted fluorene as a shielding unit (S), dialkyl-substituted cyclopentadienyl dithiophene as a donor unit (D), benzo[1,2-c:4,5-c] bis [1, 2, 5] thiadiazole (BBTD) as an acceptor (A). Additionally, the bromine atoms at the end of the alkyl chain in IR-FCD were replaced by azide groups, and the ER-targeting group, N-(but-3-yn-1-yl)-4-methylbenzenesulfonamide, was further introduced by click chemical reaction to obtain IR-FCD-Ts molecule. The relevant reaction formula and detailed structural characterizations are provided in Scheme S1 and Fig. S1-11. The water-soluble IR-FCD-Ts@DSPE-S-S-PEG2000 (IR-FCD-Ts NPs) with tumor microenvironment responsive release feature were prepared by encapsulating the hydrophobic IR-FCD-Ts with GSH-responsive DSPE-S-S-PEG2000. Additionally, IR-FCD@DSPE-S-S-PEG2000 (IR-FCD NPs), IR-FTT@DSPE-S-S-PEG2000 (IR-FTT NPs), and IR-26@DSPE-S-S-PEG2000 (IR-26 NPs) were prepared as control groups. IR-FCD-type fluorophores exhibited a substantial redshift in absorption and emission compared to IR-FTT, which could be attributed to the lower HOMO–LUMO energy gap levels in IR-FCD (Fig. 2A, C, Fig. S13, and Table 1). In the DCM environment, the absorption peaks of IR-FTT, IR-FCD, and IR-FCD-Ts are located at 890 nm, 1056 nm, and 1037 nm, respectively, and their fluorescence emission peaks are located at 1112 nm (IR-FTT), 1320 nm (IR-FCD) and 1284 nm (IR-FCD-Ts), respectively. The absorption and fluorescence redshift of IR-FCD-type fluorophores may be due to the strong conjugation and electron donating ability of dialkyl

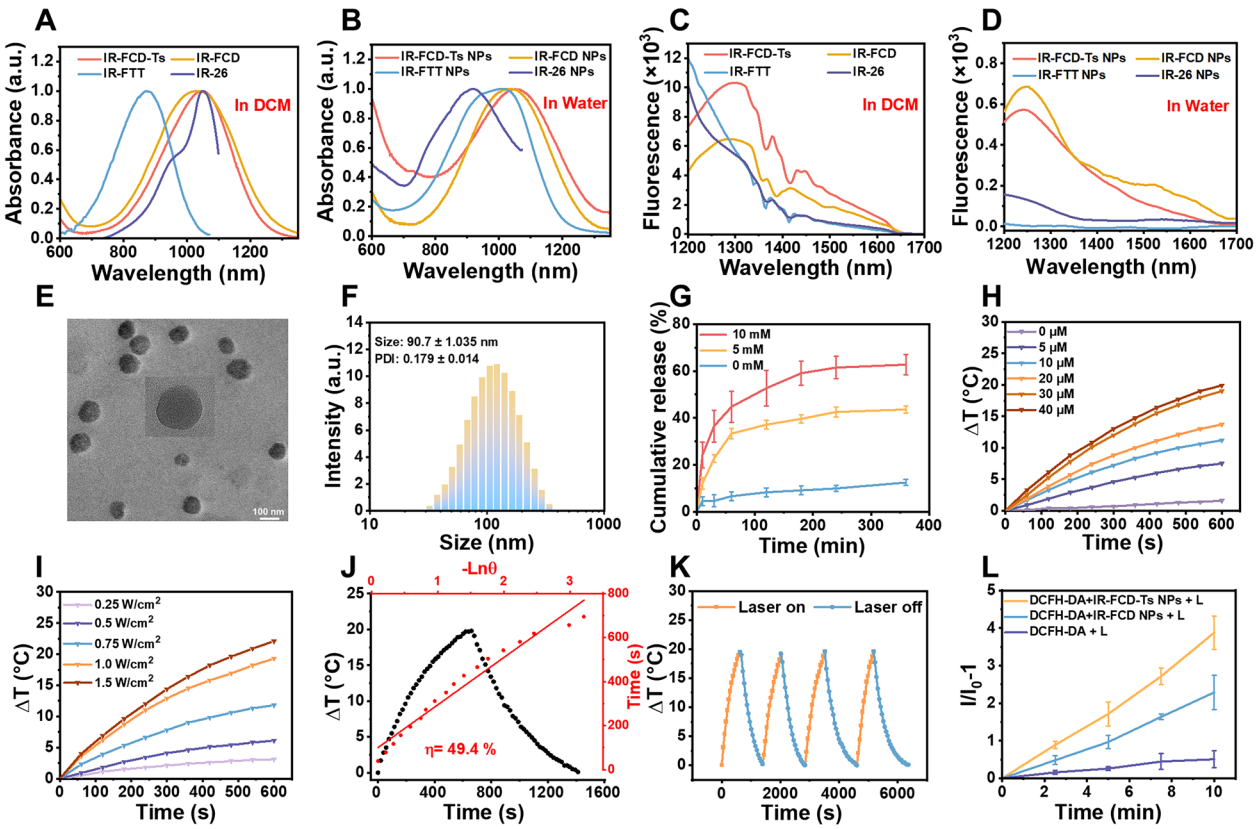

Fig. 2 **A**, **B** The absorption and **C**, **D** fluorescence emission spectra of molecular fluorophores IR-26, IR-FTT, IR-FCD, and IR-FCD-Ts in dichloromethane DCM and water solutions. **E** TEM images of IR-FCD-Ts NPs distribution analysis. **F** Hydrodynamic diameter size distribution of IR-FCD-Ts NPs. **G** Cumulative release of IR-FCD-Ts after incubating nanoparticles in GSH aqueous solutions of different concentrations for varying times. Error bars: mean ± SD (n = 3). **H** Heating curves of IR-FCD-Ts NPs at various concentrations upon 1064 nm laser irradiation. **I** Heating curve of IR-FCD-Ts NPs (30 μM) under 1064 nm laser irradiation of different power densities. **J** The photothermal conversion efficiency and **K** photothermal stability of IR-FCD-Ts NPs. **L** ROS production under 1064 nm laser irradiation with different times (I_0 and I represent the emission intensities of DCF at 525 nm before and after irradiation, respectively). Error bars: mean ± SD (n = 3)

Table 1 Optical data of NIR-II fluorophores

Dye	ε(10^3L/mol c) (1064 nm)	λ_{abs} (nm)	λ_{em} (nm)	Stokes shift (nm)	QY (%) (λex: 1064 nm)
IR-26[a]	180	1060	1110	50	0.05 ± 0.0003
IR-FTT[a]	23	890	1112	222	0.0596 ± 0.0004
IR-FCD[a]	23.7	1056	1320	264	0.0636 ± 0.0002
IR-FCD-Ts[a]	34.5	1037	1284	247	0.09375 ± 0.0002
IR-26 NPs[b]	5.3	900	1110	210	0.00199 ± 0.00003
IR-FTT NPs[b]	22	1010	–	–	0.00003 ± 0.0000004
IR-FCD NPs[b]	19.6	1058	1256	198	0.0114 ± 0.0002
IR-FCD-Ts NPs[b]	27.6	1068	1273	205	0.0088 ± 0.00002

[a] Measured in DCM

[b] Measured in water

substituted cyclopentadienyl dithiophenes enhanced the probability of an electronic transition from the ground state S_0 to the excited state S_1 (S_0–S_1 absorption). The fluorescence quantum yields (QYs) of different fluorophores in DCM were calculated to be 0.05% (IR-26), 0.0596% (IR-FTT), 0.0636% (IR-FCD), and 0.09375% (IR-FCD-Ts), respectively. The higher QYs of IR-FCD and IR-FCD-Ts can be attributed to the structural advantages of large steric hindrance from the dialkyl-substituted cyclopentadienyl dithiophenes. As shown in Fig. 2B, the extinction coefficient (ε) of IR-FCD and IR-FCD-Ts remain a high levels in water compared with IR-26 and IR-FTT (decreasing dramatically in water). Specifically, the QYs in water for different fluorophores were determined to be 0.00199% (IR-26), 0.00003% (IR-FTT), 0.0114% (IR-FCD), and 0.0088% (IR-FCD-Ts), suggesting that the IR-FCD and IR-FCD-Ts could effectively reduce fluorescence ACQ (Fig. 2D and Table 1).

The size and morphology of the resulting IR-FCD-Ts NPs were determined by dynamic light scattering (DLS) and transmission electron microscopy (TEM) measurements. As depicted in Fig. 2E, F, the IR-FCD-Ts NPs exhibited a spherical morphology with a mean hydrodynamic diameter of 90.7 ± 1.035 nm with a polydispersity index (PDI) of 0.179 ± 0.014. Notably, no significant fluctuations in size and PDI were observed even after being stored in water for 14 days (Fig. S14A), suggesting that IR-FCD-Ts NPs have good stability for biological applications. However, after incubation with 10 mM glutathione (GSH) solution for 4 h, both the size and PDI of IR-FCD-Ts NPs showed significant changes. TEM also revealed a noticeable alteration in the morphology of the IR-FCD-Ts NPs (Fig. S14B). The release of IR-FCD-Ts after incubation in various concentrations of GSH solution for different times was further tested. With the prolongation of incubation time and the increase in GSH concentration, the cumulative release of IR-FCD-Ts gradually increased. These results signify the GSH-responsive release feature of IR-FCD-Ts NPs (Fig. 2G). It is widely recognized that intracellular GSH levels in tumor cells are significantly higher than those in extracellular fluid. In addition, GSH levels in tumor tissues are usually at least four times higher than in normal tissues [44]. Thus, the GSH-responsive release of IR-FCD-Ts NPs in the tumor microenvironment could improve availability and safety.

The photothermal properties of IR-FCD-Ts NPs and IR-FCD NPs were systematically assessed. The two types of NPs demonstrate photothermal heating performances that are dependent on both concentration and laser intensity under 1064 nm laser irradiation (Fig. 2H, I and Fig. S15). Specifically, the temperature of IR-FCD-Ts NPs at 30 μM rose by over 20 °C after 10 min irradiation (1 W/cm^2), with a significant photothermal conversion efficiency (PCE) value of 49.4% (Fig. 2J). Also, IR-FCD-Ts NPs demonstrated excellent photothermal stability by four heating/cooling cycles (Fig. 2K). Subsequently, the 2′,7′-Dichlorodihydrofluorescein Diacetate (DCFH-DA) probe was used for investigating the ROS generation capacity of IR-FCD-Ts NPs. The results revealed that upon 1064 nm laser irradiation, the 2′,7′-Dichlorofluorescin (DCF) at 525 nm exhibited minimal fluorescence (Fig. 2L and Fig. S16). In contrast, in the presence of IR-FCD-Ts NPs, the fluorescence intensity of DCF at 525 nm showed a more noticeable increase with the prolongation of 1064 nm laser irradiation time. This result confirms that IR-FCD-Ts NPs possess a PDT potential.

Cellular uptake, ER-targeting imaging, cell toxicity, and apoptosis assessment

The cell uptake of IR-FCD-Ts NPs was observed using confocal laser scanning microscopy (CLSM). The results indicated that with time, the accumulation of IR-FCD-Ts NPs in tumor cells gradually increased within 4 h. After 4 h, the fluorescence intensity within the cells stabilized,

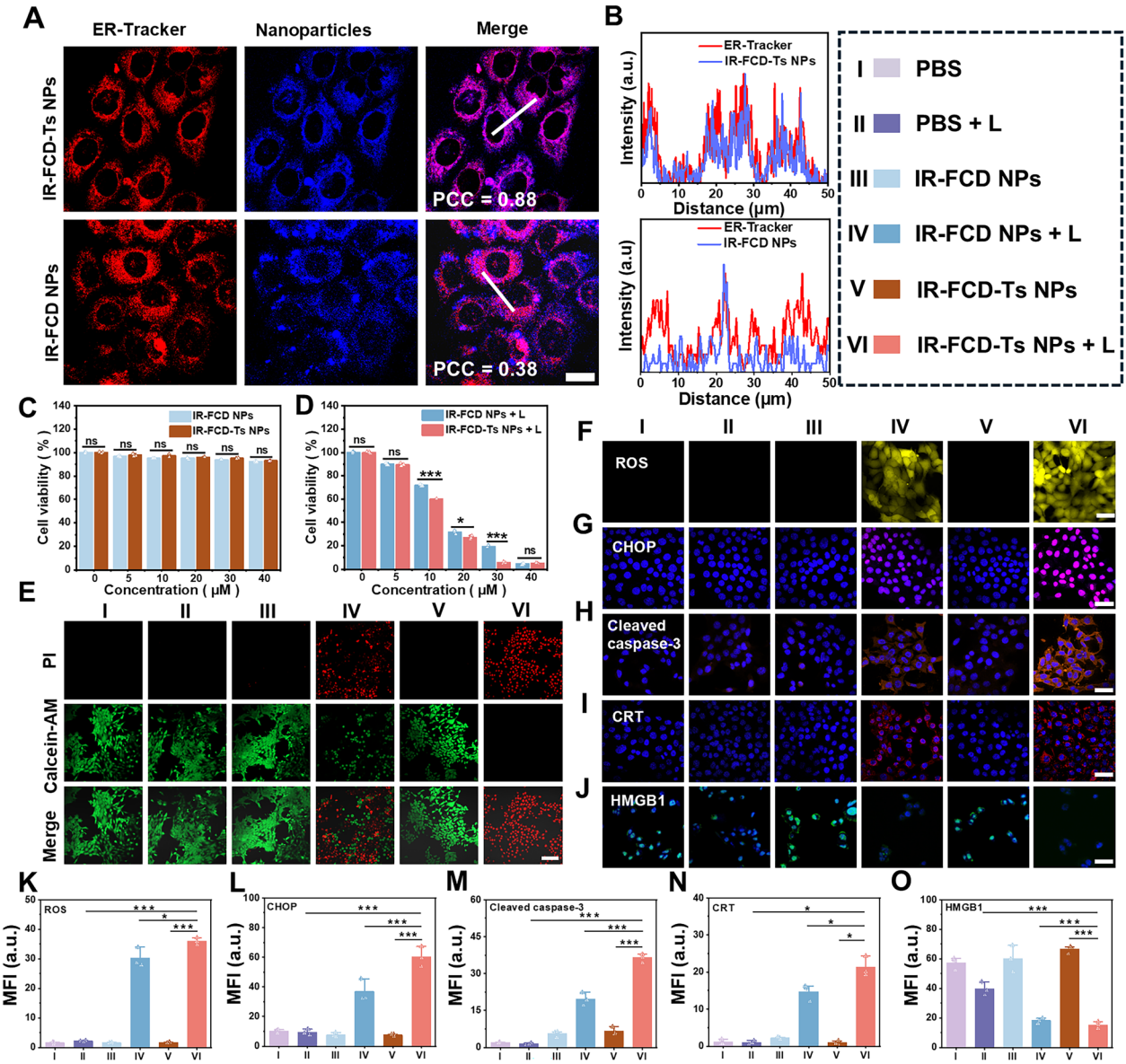

Fig. 3 **A** CLSM images of 4T1 cells following incubation with IR-FCD-Ts/IR-FCD NPs and ER-Tracker. Scale bar: 20 μm. **B** Intensity profile of linear regions of interest between IR-FCD-Ts/IR-FCD NPs and ER-Tracker. **C**, **D** Cell viability after treatment with various concentrations of IR-FCD NPs and IR-FCD-Ts NPs without/with laser irradiation (1064 nm, 1.0 W/cm^2, 10 min). Error bars: mean ± SD (n = 3). **E** Calcein-AM/PI staining after various treatments. Scale bar:100 μm. **F**–**J** CLSM images of ROS, CHOP, Cleaved Caspase-3, CRT, and HMGB1 in 4T1 cells after different treatments. Scale bar:50 μm. **K**–**O** Flow cytometric analysis of ROS, CHOP, Cleaved Caspase-3, CRT, and HMGB1 in 4T1 cells following different treatments

suggesting that the cell uptake of nanoparticles reached a saturated state (Fig. S17). Subsequently, the ER-targeted ability of IR-FCD-Ts NPs was assessed through co-localization experiments by CLSM. As revealed in Fig. 3A, B, there is a significant correlation (Pearson's correlation coefficient = 0.88) between the blue fluorescence signals of IR-FCD-Ts NPs and the red signals of ER Tracker could be determined, suggesting that IR-FCD-Ts NPs can successfully target the ER in 4T1 tumor cells. On the contrary, the IR-FCD NPs did not exhibit significant co-localization with the ER, with a Pearson's correlation coefficient of 0.38.

The phototoxicity and dark toxicity of IR-FCD-Ts NPs were assessed using Cell Counting Kit-8 (CCK-8) assays. The viability of 4T1 and HC11 cells after incubating with various concentrations of IR-FCD-Ts NPs and IR-FCD NPs were evaluated. The results confirmed that the survival rates of 4T1 and HC11 cells remained over 90%

without irradiation, even with both the NPs concentrations at over 40 μM, demonstrating minimal dark toxicity (Fig. 3C and Fig. S18). Subsequently, 4T1 cells were chosen to analyze the phototoxic effects of IR-FCD-Ts NPs. Both the laser-irradiated IR-FCD-Ts NPs and IR-FCD NPs effectively induced tumor cell death after a 10-min exposure to a 1064 nm laser at 1.0 W/cm^2. Notably, within a certain concentration range, the cell survival rates in the IR-FCD-Ts NPs group were significantly lower than those in the IR-FCD NPs group (Fig. 3D), underscoring the superior tumor cell-killing efficacy of ER-targeted IR-FCD-Ts NPs. Similar trends were observed in Calcein acetoxymethyl ester (Calcein AM) and propidium iodide (PI) staining experiments (Fig. 3E). The PBS, IR-FCD NPs, and IR-FCD-Ts NPs groups exhibited minimal impact on cell survival in the absence of a laser. However, the IR-FCD-Ts NPs + L group and IR-FCD NPs + L group exhibited significant red fluorescence after treatment, particularly, the IR-FCD-Ts NPs + L group exhibited extensive red fluorescence, suggesting robust tumor photo-ablation properties of IR-FCD-Ts NPs.

In addition, flow cytometry was used to assess the apoptosis level of 4T1 cells after different treatments. Flow cytometry analysis revealed that, compared to the other groups, the apoptosis rate of 4T1 cells in the IR-FCD-Ts NPs + L treatment group was markedly elevated (Fig. S19), which is consistent with the aforementioned research findings. Overall, these findings demonstrate that, under 1064 nm laser irradiation, IR-FCD-Ts NPs exhibit superior tumor ablation ability in vitro, providing a strong foundation for their potential anti-tumor applications in vivo.

In vitro ER stress-driven ICD mediated by IR-FCD-Ts NPs

Subsequently, we investigated the in vitro photoimmunotherapy anti-tumor mechanism mediated by IR-FCD-Ts NPs. According to previous studies [48, 49], ER-targeted phototheranostics can generate hyperthermia and ROS to cause ER protein misfolding and calcium homeostasis disruption under laser irradiation. Therefore, the generation of ROS in 4T1 cells following various treatments was assessed with a DCFH-DA probe. Flow cytometry and CLSM analysis show that 4T1 cells treated with IR-FCD-Ts NPs + L exhibit the highest fluorescence intensity, indicating efficient ROS generation (Fig. 3F, K and Fig. S20A). Sustained ER stress will cause the expression of ER stress-related proteins. The transcription factor C/EBP homologous protein (CHOP) is known to be pivotal in the process of ER stress-induced apoptosis. The CHOP levels are generally minimal in normal physiological states while substantially increased with severe ER stress [50]. Subsequently, the expression of CHOP following different treatments was assessed using immunofluorescence staining and Western blot analysis. As expected, the IR-FCD-Ts NPs + L group exhibited heightened CHOP expression (Fig. 3G, L and Fig. S20B, S21A). Meanwhile, Cleaved Caspase-3 of apoptosis-related protein was also highly expressed in the tumor cells of the IR-FCD-Ts NPs + L group (Fig. 3H, M and Fig. S20C, S21B). The above results implied that IR-FCD-Ts NPs-mediated phototherapy may provoke significant ER stress and promote tumor cell apoptosis. Based on previous research, the activation of relevant signaling pathways by ER stress significantly enhances ICD and subsequently triggers antitumor immune responses [30, 34]. ICD is associated with various DAMP events, such as the presentation of CRT on the cell surface, the extracellular release of HMGB1, and the secretion of ATP. These DAMPs play a crucial role in enhancing immune responses. For example, the CRT as a prophagocytic "eat me" signal and the ATP as a "find-me" signal collectively induce phagocytosis of apoptotic tumor cells. Additionally, the HMGB1 can stimulate DCs maturation and antigen presentation. Immunofluorescence staining and Western blotting showed that 4T1 cells in the IR-FCD-Ts NPs + L group exhibited more significant CRT exposure compared to other groups (Fig. 3I, N and Fig. S20D, S21C). Additionally, a more notable decrease was found in the HMGB1 level (Fig. 3J, O and Fig. S20E, S21D) within the cellular nucleus for the IR-FCD-Ts NPs + L group, suggesting the efflux of HMGB1 from the nucleus to the extracellular matrix during ICD. In addition, extracellular ATP assay after different treatments was detected by a commercially available ATP assay kit (Fig. S22). The results showed that IR-FCD-Ts NPs were effective in promoting ATP secretion under the irradiation of a 1064 nm laser. To sum up, ER-targeted IR-FCD-Ts NPs could effectively induce ER stress under laser irradiation and augment ICD in tumor cells, thereby further enhancing antitumor efficacy.

In vivo biocompatibility assessment, NIR-II fluorescence imaging and biodistribution

The biosafety of nanosystems is nonnegligible in its in vivo application. As shown in Fig. S23, S24, a randomized allocation assigned healthy BALB/c mice into three groups, where they received injections of PBS, IR-FCD NPs, and IR-FCD-Ts NPs via the tail vein. On day 15, the mice were euthanized, and blood analysis along with hematoxylin–eosin (H&E) staining of major organs was conducted. The results indicated that blood cell counts and biochemical parameters remained within normal ranges, and H&E sections of the major organs showed no significant abnormalities in all groups. The findings above clearly demonstrate the excellent biosecurity of both IR-FCD-Ts NPs and IR-FCD NPs. To

explore the in vivo biological distribution of IR-FCD-Ts NPs, the fluorescence imaging system was employed to track fluorescence signals at various time points (0.5, 4, 8, 12, 24, 48 h) of 4T1 tumor-bearing mice after intravenous administration of IR-FCD-Ts NPs. The fluorescence imaging revealed a gradual increase in fluorescence intensity within the tumor region, as well as in the tumor-to-normal tissue (T/N) ratio over time, both reached their peak at 24 h post-injection, followed by a slow decline (Fig. 4A, B and Fig. S25). Ex vivo fluorescence imaging analysis of harvested major organs (heart, liver, spleen, lung, kidney) and tumor tissues was conducted at 48 h post-injection (Fig. S26A, B). The results showed a higher liver and spleen accumulation compared with that of tumor tissues and other organs. The high NPs accumulation may be attributed to the high capacity of the liver and spleen for filtering and removing exogenous substances, as well as potential phagocytosis and removal via the macrophage system [51, 52]. NIR-II fluorescence imaging not only disclosed specific tumor region localization but also visualized in vivo delivery and distribution of IR-FCD-Ts NPs. To evaluate the long-term biodistribution of IR-FCD-Ts NPs, we conducted NIR-II fluorescence imaging on the major organs and excreta (feces and urine) of healthy BALB/c mice at different time points after IR-FCD-Ts NPs injection. As shown in Fig. S27, compared to day 1 post-injection, only weak fluorescence signals were detected in organs other than the liver and spleen on day 5. Furthermore, no fluorescence signal was detected in the urine, while fluorescence signals in feces, liver, and spleen persisted until day 17, indicating that IR-FCD-Ts NPs were primarily metabolized through the hepatobiliary pathway. By day 19, no fluorescence signals were detected in either the feces or major organs, suggesting that the majority of IR-FCD-Ts NPs had been metabolized in the body.

Suppressed tumor growth and metastasis by IR-FCD-Ts NPs-mediated phototherapy

Motivated by the favorable characteristics of effective tumor accumulation, phototherapy, and immunostimulatory capabilities, as well as good biocompatibility of IR-FCD-Ts NPs. In vivo antitumor properties of IR-FCD-Ts NPs were further evaluated. As depicted in Fig. 4C, 4T1 tumor-bearing mice were utilized to establish primary and distant tumor models, with the mice randomly assigned to six groups (PBS, PBS + L, IR-FCD NPs, IR-FCD NPs + L, IR-FCD-Ts NPs and IR-FCD-Ts NPs + L). The primary tumors in the irradiated groups underwent 1064 nm laser irradiation (1.0 W/cm^2 for 10 min) at 24 h post-injection. The results of in vivo photothermal analysis indicated a significant increase in temperature within the tumor region, surpassing 47 ℃ in both the IR-FCD NPs and IR-FCD-Ts NPs treatment groups (Fig. 4D). In contrast, the group treated with PBS did not exhibit a significant temperature increase.

The evaluation of in vivo antitumor efficacy over 15 days revealed a notable increase in tumor volume and weight for both primary and distant tumors in the PBS, IR-FCD NPs, and IR-FCD-Ts NPs groups without laser irradiation. However, both the volume and weight of the primary and distant tumors in the IR-FCD NPs + L group exhibited a slow-growing trend. Encouragingly, there was almost no increase in tumor volume in the IR-FCD-Ts NPs + L group, and the inhibition rates of primary and distant tumors were 94.3% and 80.6%, respectively (Fig. 4E–G and Fig.S28, S29). As shown in Fig. S30, the H&E, TUNEL (Terminal deoxynucleotidyl transferase dUTP nick-end labeling), and Ki-67 staining of the post-treatment tumor tissues in IR-FCD-Ts NPs + L group revealed severe cell necrosis, nucleolysis, increased apoptotic, and reduced proliferation compared with other groups. The above data confirms that IR-FCD-Ts NPs showed a superior antitumor effect under 1064 nm laser irradiation.

Extensive metastasis is the primary cause of cancer-related deaths [53]. Metastasis suppression is the key to improving the outcome of cancer treatment. Consequently, we further evaluated the inhibition of lung metastasis by IR-FCD-Ts NPs-mediated phototherapy. Following phototherapy of subcutaneous tumors, 4T1 cells were injected into 4T1 tumor-bearing mice via the tail vein to establish a metastasis model (Fig. 4H). Lung metastasis was assessed on day 21 after laser irradiation. As shown in Fig. 4I and Fig. S31, metastatic nodules could be observed in the lung tissues of all groups, while the IR-FCD-Ts NPs + L and IR-FCD NPs + L groups demonstrated significantly fewer metastatic nodules, with the IR-FCD-Ts NPs + L group showing the fewest lung metastatic nodules compared to other groups. The above results were also supported by H&E-stained lung tissue sections (Fig. 4J). These results reflect the superior inhibitory effect of IR-FCD-Ts NPs-mediated phototherapy on lung metastasis under 1064nm laser irradiation.

In vivo antitumor immune activation mediated by IR-FCD-Ts NPs

The IR-FCD-Ts NPs-mediated photoimmunotherapy in vivo was further investigated through immunofluorescence staining (Fig. 5A). Initially, the expression of CHOP in tumor tissues of different groups was explored. The results showed that, compared to the IR-FCD NPs + L group, the CHOP expression in the ER-targeted IR-FCD-Ts NPs + L group was significantly increased, while no obvious CHOP expression was observed in the other groups. Then, the critical apoptotic protein Cleaved

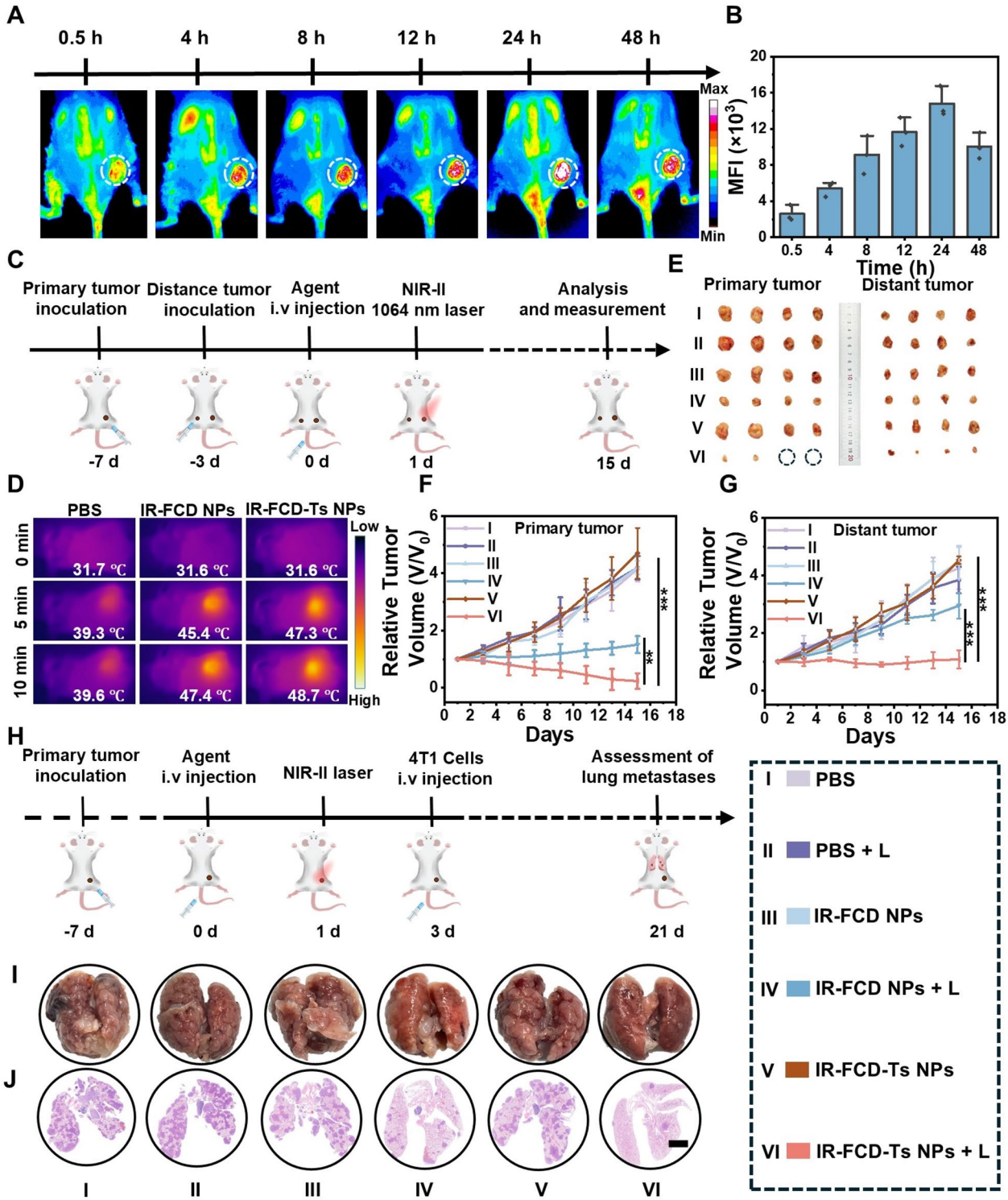

Fig. 4 **A** Fluorescence images in real-time of 4T1 tumor-bearing mice following intravenous administration of IR-FCD-Ts NPs at various time intervals. **B** The fluorescence intensity of tumors was quantified at various time points following injection. **C** Schematic representation of in vivo antitumor therapy. **D** Photothermal images of 4T1 tumor-bearing mice after different treatments 24 h with 1064 nm laser irradiation (1.0 W/cm^2, 10 min). **E** Representative tumor photographs were collected from mice with different treatments (day 15). The relative tumor volumes in different treatment groups of the **F** primary and **G** distant tumor. **H** The schematic diagram of anti-lung metastasis treatment. **I** Representative images of the lung tissues after different treatments. **J** H&E-staining of lung tissues after different treatments. Scale bar: 500 μm. Error bars, mean ± SD (n = 3)

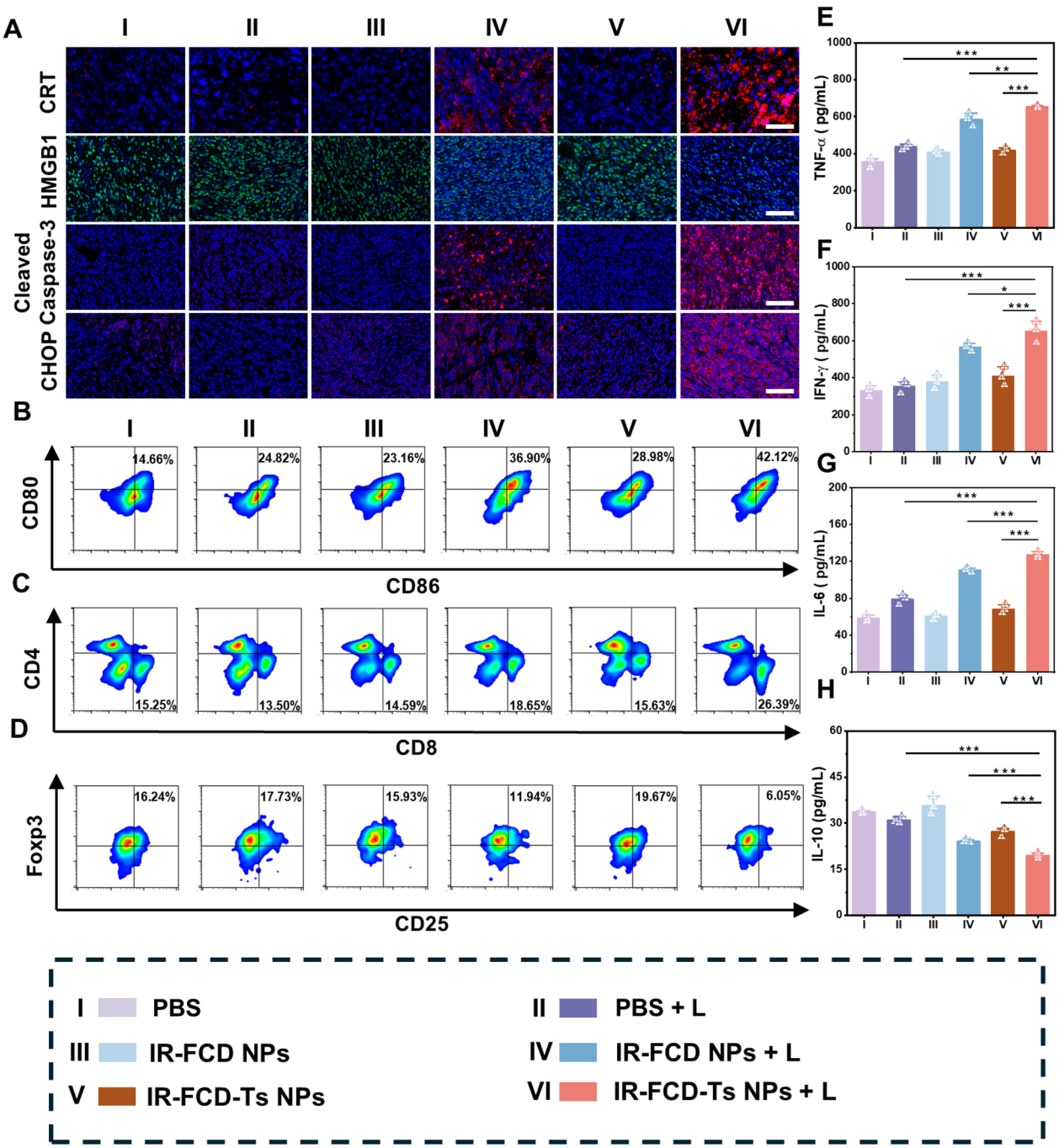

Fig. 5 **A** CHOP, Cleaved Caspase-3, CRT, HMGB1 staining of the primary tumor tissues after various treatments. The representative flow cytometric analyses of **B** DCs ($CD80^+$ $CD86^+$ $CD11C^+$), **C** CTLs ($CD3^+$ $CD8^+$), and **D** Tregs ($CD4^+$ $CD25^+$ $Foxp3^+$) in primary tumors from 4T1 tumor-bearing mice after different treatments. **E**–**H** TNF-α, IFN-γ, IL-6, and IL-10 levels of 4T1 tumor-bearing BALB/c mice after different treatments. Error bars: mean ± SD (n = 3)

Caspase-3 in tumor tissues was evaluated. Consistently, immune fluorescence staining within the IR-FCD-Ts NPs + L group exhibited the highest expression of Cleaved Caspase-3.

Subsequently, the ICD-related molecules, CRT and HMGB1, were further investigated. Immunofluorescence staining results revealed that compared to the other groups, both the IR-FCD NPs + L group and

the IR-FCD-Ts NPs + L group exhibited elevated CRT expression and reduced HMGB1 expression. Notably, the IR-FCD-Ts NPs + L group demonstrated significantly higher CRT exposure and HMGB1 release than the IR-FCD NPs + L group. These findings suggest that, under 1064 nm laser irradiation, IR-FCD-Ts NPs enhance the ICD effect via the ER stress pathway.

To assess the systemic immune response after treatment, the immune cells from tumor and spleen tissues, along with cytokines from serum, were collected for analysis. Firstly, DCs, as a crucial hallmark, were investigated. Flow cytometric analysis of DCs within the primary tumor tissue post-treatment revealed a noteworthy increase of mature DCs in the IR-FCD-Ts NPs + L group compared to PBS and IR-FCD-Ts NPs groups (Fig. 5B and Fig. S34A), meaning potentially enhanced activation of T-cell immunity. As depicted in Fig. 5C and Fig. S34B, the IR-FCD-Ts NPs + L group displayed a significant augmentation of CTLs ($CD8^+$ T cells) within tumor tissues. Correspondingly, the proportion of regulatory T cells (Tregs) was significantly reduced (Fig. 5D and Fig. S34C). Immunofluorescence staining results further indicated that the IR-FCD-Ts NPs + L group displayed the highest level of $CD8^+$ T cell infiltration and the reduced population of Tregs (Fig. S32). Meanwhile, the levels of anticancer-involved cytokines IL-6, IFN-γ, and TNF-α were found to be up-regulated in the IR-FCD-Ts NPs + L groups (Fig. 5E–G) with significantly decreased tumor-promoting cytokine IL-10 (Fig. 5H). The promising antitumor immune activation of IR-FCD-Ts NPs in eliminating primary tumors prompted us to investigate its therapeutic potential for metastatic tumors through photoimmunotherapy. As we expected, based on flow cytometry (Fig. S33 and Fig. S34D, E), compared to the other groups, both the IR-FCD NPs + L group and IR-FCD-Ts NPs + L group showed an increase in memory T cells, while the IR-FCD-Ts NPs + L group demonstrated a significantly higher proportion of immune memory T cells in both distant tumor tissues and the spleen. Moreover, immunofluorescence staining revealed a substantial increase in $CD8^+$ cells in both distant tumors and spleen tissues of the IR-FCD-Ts NPs + L group (Fig. S35). These findings indicate that under 1064 nm laser irradiation, IR-FCD-Ts NPs activated an in vivo antitumor immune response through ER stress amplified ICD, which in turn inhibited the metastasis of TNBC.

Conclusions

In summary, we propose a novel molecular design strategy by introducing di-hexaalkyl chains with a vertical configuration and large steric hindrance on the donor (4H-cyclopenta [2,1-b: 3,4-b'] dithiophene) to construct an S-D-A-D-S typed NIR-II phototheranostics (IR-FCD). The planar and rigid IR-FCD with a robust intramolecular charge transfer ability, a lower band gap, and enhanced photon absorption ability. Moreover, large steric hindrance from the alkyl chains in IR-FCD could attenuate the intermolecular π–π stacking interaction to minimize the loss of non-radiative energy, which results in strong fluorescence emission performance in the aggregation state. Formation of NIR-II excitable phototheranostics (IR-FCD-Ts NPs) with ER-targeting by incorporation of N-(but-3-yn-1-yl)-4-methylbenzenesulfonamide at the end of an elongated alkyl chain and self-assembly with DSPE-S-S-PEG2000: for NIR-II imaging-guided ER-targeted TNBC photoimmunotherapy. Encouragingly, the IR-FCD-Ts NPs exhibit excellent biocompatibility and selectively accumulate in the ER, enabling NIR-II fluorescence imaging-guided PTT and PDT treatment. Furthermore, IR-FCD-Ts NPs-mediated ER-targeted phototherapy enhances ICD, activates antitumor immune responses, and effectively inhibits the proliferation and metastasis of TNBC. However, there are still some limitations in this study that need to be further considered. Firstly, under the irradiation of the 1064 nm laser, although the IR-FCD-Ts NPs have the potential for PDT, their ROS generation capacity is relatively weak due to the influence of competitive photophysical mechanisms. Therefore, future research could explore ways to further optimize the photophysical process to enhance ROS generation efficiency. Secondly, this study was conducted only in a subcutaneous tumor model. While this model has certain representativeness in preliminary evaluations, it may not fully reflect the complexity and diversity of tumors in clinical settings. Therefore, using an orthotopic TNBC tumor model for research might be more helpful in assessing the clinical translational potential and therapeutic efficacy of IR-FCD-Ts NPs. Despite these limitations, overall, this study presents a promising strategy for effectively treating TNBC.

Experimental section

Materials and reagents

2-Bromofluorene, KOH, NaOH, tetrabutylammoniumbromide, 2-(tributysltannyl) thiophene, Tetrakis(triphenylphosphine)palladium, 1,6-dibromohexane, Toluene, N-Bromosuccinimide, N, N-Dimethylformamide, 6-Bromo-1-hexanol, $NaHSO_4$, Tetrahy- drofuran, n-Butyllithium, Tributyltin chloride, Bis(triphenylphosphine) palladium(II) Dichloride, 4, 7-dibroMobenzo[1, 2-c:4, 5 c']bis([1, 2, 5]thiadiazole), 3, 4-Dithia-7H cyclopenta[a]pentalene. DSPE-S-S-PEG2000 was purchased from Xi'an Ruixi Biotech Co., Ltd. Cell Counting Kit-8 (CCK-8) was provided by Dojindo Co., Ltd. ER Tracker Red was purchased from Key GEN BioTECH Corp., Ltd. The Annexin V-FITC/PI kit was

purchased from Meilun Biotechnology Co., Ltd. The Calreticulin (CRT) antibody and High Mobility Group Box 1 (HMGB1) antibodies were purchased from Abcam Co. Ltd. The C/EBP Homologous Protein (CHOP) antibody was purchased from Diagbio Biotechnology Co., Ltd. The Cleaved Caspase-3 antibody was purchased from Zenbio Biotechnology Co., Ltd. D-propargylglycine, and 2,7-Dichlorodihydrofluorescein diacetate (DCFH-DA) was purchased from Sigma-Aldrich Co., Ltd. Calcein acetoxymethyl ester (Calcein AM), propidium iodide (PI) assay kit was provided by Nanjing Vazyme BioTech Co., Ltd. The flow cytometry antibodies for mouse immune cell analysis were purchased from Elabscience® Biotechnology Co., Ltd. The 4T1 mouse mammary carcinoma cells and HC11 mouse mammary epithelial cells were procured from the American Type Culture Collection (ATCC) and subsequently cultured in Dulbecco's Modified Eagle Medium (DMEM, Hyclone), supplemented with 10% fetal bovine serum (FBS, ExCell Bio, Shanghai, China), at 37 °C in a humidified atmosphere containing 5% CO_2.

General measurements

High-resolution mass spectra (HRMS) were acquired using a Thermo Scientific Q Exactive quadrupole Orbitrap mass spectrometer (Thermo Fisher Scientific Co., USA) operating in positive ion mode. A spectrometer was used to measure the UV − Vis − NIR absorption spectra (MAPADA UV-3200S, Shanghai, China). The Near-infrared II fluorescence spectroscopy was measured via a Fiber optic spectrometer (NIR-17S, Shanghai ideaoptics Co, China). Confocal laser scanning microscopy (CLSM) images were taken using Zeiss LSM980 (Zeiss, Germany). Flow cytometric analysis was conducted on flow cytometry (FCM, Agilent, China). The fluorescence spectra were recorded using a Thermo Scientific Lumina fluorescence spectrometer.

Glutathione-stimulated release

To evaluate the responsive release of IR-FCD-Ts in glutathione (GSH), solutions containing 10 mL of 30 μM IR-FCD-Ts nanoparticles were incubated with GSH at different concentrations over varying durations (0, 10, 30, 60, 120, 180, 240, and 360 min). At each time point, 1 mL of the nanoparticle dispersion was sampled, followed by centrifugation at 9000 rpm for 10 min, and the IR-FCD-Ts released into the supernatant were determined by UV–Vis spectroscopy.

ROS detection in aqueous solution

The ROS was detected utilizing the probe DCFH-DA. Laser irradiation of IR-FCD-Ts NPs induced the production of ROS, followed by the detection of fluorescence intensity at 525 nm using a fluorescence spectrophotometer (excitation wavelength: 488 nm).

Photothermal performance of IR-FCD-Ts NPs

Temperature changes (IR-FCD-Ts NPs, solvent: water) under 1064 nm laser irradiation at various concentrations and power densities were monitored using an infrared image camera. The photothermal stability of IR-FCD-Ts NPs in an aqueous solution was assessed by monitoring temperature changes during irradiation with a 1064 nm laser (1.0 W/cm^2, 10 min) and subsequent natural cooling to room temperature through four heating/cooling cycles.

To assess the photothermal conversion efficiency (η), the IR-FCD-Ts NPs solution (30 μM) was subjected to a laser exposure of 1.0 W/cm^2 for 10 min. Subsequently, the solution was cooled to the ambient temperature by shutting off the laser. In addition, IR thermal cameras were used for recording the temperature, and ultrapure water was used as a control.

The following formula was frequently used to calculate η:

It was calculated according to Eqs. (1)–(5).

$$\eta = \frac{hS(T_{max} - T_{surr}) - Q_0}{I(1 - 10^{-A_\lambda})} \tag{1}$$

the following equation can calculate hS:

$$hS = \frac{\sum m_i C_{P.i}}{\tau_s} \tag{2}$$

$$\tau_s = \frac{\mathrm{t}}{-\ln\theta} \tag{3}$$

$$\theta = \frac{T - T_{surr}}{T_{max} - T_{surr}} \tag{4}$$

$$Q_0 = \mathrm{hs}(T_{max} - T_{surr}) \tag{5}$$

h represents the heat transfer coefficient,

s represents the sample container surface area,

T_{max} represents the steady-state maximum temperature,

T_{surr} represents the ambient room temperature,

T represents instantaneous temperature during cooling,

t represents the time it takes for T to cool to room temperature,

C approximate to the specific heat capacity of water,

m represented the mass of the solution (g),

Q_0 represents the energy input by the same solvent without NPs in the same quartz cuvette after the same laser irradiation.

Cell uptake experiment

To determine the cellular uptake of IR-FCD-Ts NPs in 4T1 tumor cells, we conducted a time-course analysis using CLSM. Specifically, 4T1 cells were seeded (1×10^5 cells per dish) and incubated overnight at 37 ℃, and then treated with IR-FCD-Ts NPs (30 μM) for varying durations (0, 2, 4, 6, 8, and 12 h) before being examined using CLSM.

In vitro assessment of ER targeting capacity

Initially, 4T1 cells were seeded and cultured overnight in a confocal dish. Subsequently, the cells were exposed to IR-FCD-Ts NPs and IR-FCD NPs at a concentration of 30 μM for 4 h. Post-treatment, the cells underwent three washes with PBS and were subsequently stained with a commercial ER-Tracker Red probe at a concentration of 1 μM for 30 min. The stained cells were then analyzed using CLSM.

CCK8 assay

The cytotoxic effects of nanoparticles were assessed using the CCK8 assay, which included evaluations of both cellular dark toxicity and phototoxicity. To assess dark toxicity, 4T1 and HC11 cells were plated onto 96-well culture plates (1×10^4 cells per well) and allowed to incubate for 24 h. Subsequently, the cells were incubated with varying concentrations (0, 5, 10, 20, 30, and 40 μM) of IR-FCD NPs and IR-FCD-Ts NPs for a duration of 4 h. Cell viability was then quantified using the CCK8 assay. To confirm the phototoxic effects of IR-FCD NPs and IR-FCD-Ts NPs, cells were treated with different concentrations (0, 5, 10, 20, 30, and 40 μM) of nanoparticles and then exposed to a 1064 nm laser at a power density of 1.0 W/cm^2 for 10 min. Subsequently, cell viability was evaluated using the CCK8 assay after an additional 24 h incubation.

Calcein AM/PI staining

4T1 cells were first cultured in confocal chambers (1×10^5 cells per dish) overnight. The cells were then allocated into six groups based on different treatments, including PBS, PBS + L, IR-FCD NPs, IR-FCD NPs + L, IR-FCD-Ts NPs, IR-FCD-Ts NPs + L, with a nanoparticle concentration of 30 μM. + L represents 1064 nm laser irradiation at 1.0 W/cm^2 for 10 min. Subsequently, residual nanoparticles were removed by washing the cells three times with PBS. After a 4 h incubation period, AM (1 μM) and PI (1 μM) were introduced to each group of cells for 30 min, followed by observation using CLSM.

Assessment of cellular apoptosis

To quantify the apoptotic status of cells, 4T1 cells were seeded in 12-well plates at a density of 1.2×10^5/well and cultured overnight. The cells were divided into six groups: PBS, PBS + L, IR-FCD NPs, IR-FCD NPs + L, IR-FCD-Ts NPs, IR-FCD-Ts NPs + L with a nanoparticle concentration of 30 μM. + L represents 1064 nm laser irradiation at 1.0 W/cm^2 for 10 min. After different treatments, the cells were cultured for another 4 h washed with PBS, and trypsinized to afford single-cell suspensions. The cells were stained with the annexin V–FITC apoptosis detection kit and then analyzed by flow cytometry.

Intracellular ROS detection

To monitor ROS production in cells, DCFH-DA was utilized. The 4T1 cells after incubation in confocal chambers were divided into six distinct experimental groups: PBS, PBS + L, IR-FCD NPs (30 μM), IR-FCD NPs + L, IR-FCD-Ts NPs (30 μM), IR-FCD-Ts NPs + L. + L represents 1064 nm laser irradiation at 1.0 W/cm^2 for 10 min. The various cell groups were incubated with nanoparticles and PBS for 4 h, then washed thrice with PBS. Subsequently, they were treated with DCFH-DA (10 μM) for 30 min, followed by exposure to a 1064 nm laser for 10 min in the laser irradiation group. Post-treatment, the cells were analyzed using CLSM and flow cytometry. The CLSM images were imported into ImageJ software for fluorescence intensity quantification analysis.

In vitro assessment of CHOP, cleaved caspase-3, CRT, and HMGB1 expression

4T1 cells were treated with PBS, IR-FCD NPs (30 μM), or IR-FCD-Ts NPs (30 μM) for 4 h, with or without exposure to a 1064 nm laser (1W/cm^2, 10 min). After treatment, the cells were fixed with a 4% paraformaldehyde solution for 15 min. Excess protein binding sites were blocked by incubating the cells in a blocking buffer for 60 min. The cells were then incubated with primary antibodies against CRT, HMGB1, CHOP, and Cleaved Caspase-3 for 2 h. Following this, the cells were treated with the appropriate secondary antibodies for 1 h at room temperature. Then, the cells were analyzed by flow cytometry, or stained with DAPI and observed under a CLSM. CLSM images were imported into ImageJ software for fluorescence intensity quantification analysis.

Western blotting was also performed to evaluate the expression of CHOP, Cleaved Caspase-3, CRT, and HMGB1, with β-actin as the reference. 4T1 cells were seeded in 6-well plates (2×10^5 cells/well) and incubated overnight. When the cell density reached 60%−70%, they were randomly divided into six groups: PBS, PBS + L, IR-FCD NPs (30 μM), IR-FCD NPs + L, IR-FCD-Ts NPs

(30 μM), IR-FCD-Ts NPs + L. + L represents 1064 nm laser irradiation at 1.0 W/cm^2 for 10 min. After different treatments, the cells were cultured for an additional 24 h. The culture medium was aspirated, and the cells were washed twice with cold PBS. Radioimmunoprecipitation assay (RIPA) lysis buffer was added on ice. After grinding, the cell lysates were collected and centrifuged at 4 °C (12,000×*g* for 15 min). The proteins in the supernatant were separated by Sodium Dodecyl Sulfate Polyacrylamide Gel Electrophoresis (SDS-PAGE) and transferred to a Polyvinylidene Fluoride (PVDF) membrane. The membrane was blocked with 5% non-fat milk in TBST buffer for 2 h. The membrane was then incubated overnight at 4 °C with diluted antibodies against CRT (1:1000), HMGB1 (1:10000), CHOP (1:1000), and Cleaved-Caspase3 (1:1000). After thorough washing with TBST, the membrane was incubated at room temperature for 2 h with horseradish peroxidase-conjugated secondary antibody. After washing off the secondary antibody, the membrane was incubated with chemiluminescent reagent (MA0186-2, Meilunbio) and imaged by the FluorChem R system (Baygene, Beijing, China).

Extracellular ATP assay

4T1 cells were seeded and incubated overnight, and then divided into six groups based on different treatments: PBS, PBS + L, IR-FCD NPs, IR-FCD NPs + L, IR-FCD-Ts NPs, and IR-FCD-Ts NPs + L. + L represents 1064 nm laser irradiation at 1.0 W/cm^2 for 10 min. After different treatments and incubation for 2 h. The cell supernatant was collected into a centrifuge tube and centrifuged at 12,000×*g* for 5 min at 4 °C. Then, 100 μL of ATP working solution was added to a black 96-well plate and allowed to incubate for 5 min. Subsequently, 20 μL of the sample and standard were added sequentially, mixed thoroughly, and detected using a luminometer. The ATP content was calculated according to the instructions.

Animals

Female BALB/c mice, aged 4 to 5 weeks, were obtained from Hunan SJA Laboratory Animal Co., Ltd. All animal procedures were approved by the University of South China and followed ethical guidelines for animal experimentation and health protocols founded by national institutes for the care and use of laboratory animals.

Evaluation of systemic toxicity in vivo

To assess the in vivo biocompatibility, female BALB/c mice were divided into three groups. Each group received intravenous injections of PBS (100 μL), IR-FCD NPs (100 μL, 300 μM), and IR-FCD-Ts NPs (100 μL, 300 μM), respectively. After day 15, the blood samples of the mice were collected from each cohort for a comprehensive biochemistry analysis and complete blood count to assess the potential long-term biotoxicity of the nanoparticles. Following blood collection, the mice were euthanized, and major organs were harvested for pathological examination with hematoxylin and eosin (H&E) staining.

NIR-II fluorescence imaging and biodistribution

A suspension containing 2×10^6 4T1 cells was injected subcutaneously into the right dorsal side of the female BALB/c mice (4 to 5 weeks). Once the tumor volume reached approximately 120 mm^3, IR-FCD-Ts NPs (300 μM, 100 μL) were administered via intravenous injection. Then, NIR-II fluorescence images of the mice were captured at various time points post-injection (0.5, 4, 8, 12, 24, 48 h) by a NIR-II fluorescence imaging system (Raptor Photonics, Ninox-640 SU). To assess the distribution of IR-FCD-Ts NPs, the mice were euthanized 48 h after injection. Major organs and tumor tissues were collected for ex vivo fluorescence imaging analysis. Fluorescence intensity was quantified using the analysis tools in ImageJ, and the corresponding values were recorded. The quantified data were then saved and organized for subsequent analysis. Furthermore, to assess the long-term biodistribution of nanoparticles, NIR-II fluorescence imaging was performed on major organs and excretion collected at different time points after injecting healthy BALB/c mice with IR-FCD-Ts NPs.

In vivo antitumor therapy and immune response.

4T1 cells suspension were inoculated subcutaneously into the right dorsal side of mice (primary tumor), after 4 days, 4T1 cells were inoculated subcutaneously into the left side of mice (distant tumor). When the primary tumor volume of the mice grew to approximately 120 mm^3, the mice were randomly divided into six groups (PBS, PBS + L, IR-FCD NPs, IR-FCD NPs + L, IR-FCD-Ts NPs, IR-FCD-Ts NPs + L. + L represents 1064 nm laser irradiation at 1.0 W/cm^2 for 10 min). Afterwards, PBS (100 μL) and NPs (300 μM, 100 μL) were injected through the tail vein. For laser irradiation groups, the mice were treated with a 1064 nm laser for 10 min at 1 W/cm^2 after 24 h. The primary and distant tumor volumes of the mice were monitored every other day after treatments. which were estimated by the formula of $V = (\text{tumor length}) \times (\text{tumor width})^2/2$.

To evaluate the antitumor immune effects, the mice were euthanized on day 15 following various treatments. Firstly, serum samples were collected from the mice to measure various cytokines (TNF-α, IL-6, IFN-γ, and IL-10) using an Enzyme-Linked Immunosorbent Assay (ELISA) kit. Subsequently, spleen, primary tumors, and distant tumors were collected. The tumors and spleen were chopped into small fragments

and placed in a 70 μm cell strainer, which was set in a 6-well plate. The tissues were then disrupted mechanically using a 5 mL syringe plunger to generate a single-cell suspension, followed by homogenization in PBS and filtration to isolate individual cells. Red blood cells were removed by applying a specific lysis buffer. Finally, spleen lymphocytes were separated by passing the minced tissue through a 70 μm cell strainer. To assess dendritic cell (DC) maturation, cell suspensions obtained from primary tumors were labeled with PE Anti-Mouse CD11c, APC-Anti-Mouse CD80, and FITC-Anti-Mouse CD86 antibodies and subsequently analyzed using flow cytometry. Cytotoxic T-lymphocytes (CTLs) were examined by staining cell suspensions from primary tumors with PE-Anti-Mouse CD4, FITC-Anti-Mouse CD8a, PerCP/Cyanine 5.5 Anti-Mouse CD3 antibodies, followed by flow cytometry analysis, and subsequently analyzed using flow cytometry. For regulatory T cells (Tregs) analysis, cell suspensions from the primary tumors were first stained with PerCP/Cyanine 5.5 Anti-Mouse CD3, PE-Anti-Mouse CD4, and FITC-Anti-Mouse CD25 antibodies. Subsequently, the suspension was further stained with APC -Anti-Mouse Foxp3 antibodies before being analyzed using flow cytometry.

Memory T cell analysis was also conducted by sacrificing mice after receiving different treatments (PBS, PBS + L, IR-FCD NPs, IR-FCD NPs + L, IR-FCD-Ts NPs, IR-FCD-Ts NPs + L. + L represents 1064 nm laser irradiation at 1.0 W/cm^2 for 10 min). Spleens and distant tumors were harvested, homogenized in PBS, and filtered to isolate single-cell suspensions. The splenocytes and tumor cells were then labeled with FITC Anti-Mouse CD8a, APC Anti-Human/Mouse CD44, and PE/Cyanine 7 Anti-Mouse CD62L antibodies subsequently analyzed using flow cytometry.

To evaluate the effectiveness of IR-FCD-Ts NPs-mediated photo-immunotherapy in addressing lung metastasis of TNBC, we established a delay lung metastasis model. Initially, 4T1 (2×10^6) cells were subcutaneously injected into the right dorsal side of mice. Once the tumors reached approximately 120 mm^3 in volume, the mice were randomly assigned to one of six groups: (PBS, PBS + L, IR-FCD NPs, IR-FCD NPs + L, IR-FCD-Ts NPs, IR-FCD-Ts NPs + L. + L represents 1064 nm laser irradiation at 1.0 W/cm^2 for 10 min). On day 0, PBS (100 μL) or nanoparticles (300 μM, 100 μL) were administered intravenously via the tail vein. After 24 h, the tumors were exposed to a 1064 nm laser at 1W/cm^2 for 10 min. On day 3, 4T1 cells (2×10^5) were injected into mice via the tail vein. At the end of the observation period, the mice were euthanized, and pulmonary metastatic nodules were analyzed.

Histological analysis

BALB/c mice that underwent various treatments (PBS, PBS + L, IR-FCD NPs, IR-FCD NPs + L, IR-FCD-Ts NPs, IR-FCD-Ts NPs + L. + L represents 1064 nm laser irradiation at 1.0 W/cm^2 for 10 min) were euthanized on day 15 to harvest major organs and tumors for histological analysis. The organs, including the heart, liver, spleen, lung, and kidney, were subjected to staining with H&E. Tumor sections treated with different agents were also stained with H&E, terminal deoxynucleotidyl transferase-mediated dUTP nick-end labeling (TUNEL), Ki-67, CRT, HMGB1, Cleaved Caspase-3, CHOP, CD8$^+$T, and Treg markers for further examination.

Statistical analysis

Statistical analysis was conducted using SPSS version 25.0, employing Student's t-test and one-way analysis of variance (ANOVA). Results are presented as mean ± standard deviation (SD) from experiments repeated more than three times. Statistical significance was defined as $P<0.05$. Significance levels are denoted as follows: $^*P<0.05$, $^{**}P<0.01$, $^{***}P<0.001$; "ns" represents no statistically significant difference.

Abbreviations

TNBC	Triple-negative breast cancer
NIR-I	The first near-infrared
UV–Vis	Ultraviolet–visible
ICD	Immunogenic cell death
TAAs	Tumor-associated antigens
DAMPs	Damage-associated molecular patterns
CRT	Calreticulin
HMGB1	High-mobility group box1
ATP	Adenosine triphosphate
DCs	Dendritic cells
CTLs	Cytotoxic T-lymphocytes
IFN-γ	Interferon-γ
TNF-α	Tumor necrosis factor-α
IL	Interleukins
EDOT	Ethylenedioxy-thiophene
NIR-II	The second near-infrared
MPE	Maximum permissible exposure
ROS	Reactive oxygen species
BODIPY	Boron dipyrromethene
ACQ	Aggregation-caused quenching
D-A-D	Donor–acceptor–donor
D-A	Donor–acceptor
MD	Molecular dynamics
ER	Endoplasmic reticulum
DFT	Density functional theory
TDDFT	Time-dependent density functional theory
BBTD	Benzobisthiadiazole
HOMO	Highest occupied molecular orbital
LOMO	Lowest unoccupied molecular orbital
DLS	Dynamic light scattering
TEM	Transmission electron microscopy
GSH	Glutathione
PCE	Photothermal conversion efficiency
CCK-8	Cell Counting Kit-8
DCFH-DA	2,7-Dichlorodi-hydrofluorescein diacetate
DCF	2′,7′-Dichlorofluorescin
Calcein AM	Calcein acetoxymethyl ester

PI	Propidium ioniudide
Tregs	Regulatory T cells
CHOP	C/EBP homologous protein
RIPA	Radioimmunoprecipitation assay
SDS-PAGE	Sodium Dodecyl Sulfate Polyacrylamide Gel Electrophoresis
PVDF	Polyvinylidene Fluoride
H&E	Hematoxylin–eosin
TUNEL	TdT-mediated dUTP nick end labeling assays
ELISA	Enzyme-Linked Immunosorbent Assay

Supplementary Information

The online version contains supplementary material available at https://doi.org/10.1186/s12951-025-03282-5.

Additional file 1: Fig. S1 ^{1}H NMR of compound 4. Fig. S2 ^{13}C NMR of compound 4. Fig. S3 HRMS of compound 4. Fig. S4 ^{1}H NMR of compound 6. Fig. S5 ^{13}C NMR of compound 6. Fig. S6 HRMS of compound 6. Fig. S7 ^{1}H NMR of compound 8. Fig. S8 ^{13}C NMR of compound 8. Fig. S9 HRMS of compound 8. Fig. S10 ^{1}H NMR of compound 9. Fig. S11 ^{13}C NMR of compound 9. Fig. S12 Absorption spectra of (A) IR-FTT and (B) IR-FCD in DCM and water, respectively. Fig. S13 The absorption spectra (300-1300 nm) of molecular fluorophores IR-26, IR-FTT, IR-FCD, and IR-FCD-Ts in (A) DCM and (B) water. Fig. S14 (A) Size and PDI stability of IR-FCD-Ts NPs in deionized water for 14 days. (B) DLS and TEM of IR-FCD-Ts NPs after 4 h incubation with 10 mM GSH solution. Fig. S15 (A) The temperature changes of different concentrations of IR-FCD NPs under 1064 nm laser irradiation (1.0 W/cm^2). (B) Heating curve of IR-FCD NPs (30 μM) under 1064 nm laser irradiation of different power densities. Fig. S16 (A-C) ROS production by nanoparticles was assessed under 1064 nm laser irradiation at different time points.Fig. S17 (A) Cellular uptake of IR-FCD-Ts NPs by 4T1 cells at different incubation times. Scale bar: 50 μm. (B) The MFI data of (A). Error bars, mean ± SD (n = 3). Fig. S18 Cell viability of HC11 cells after incubating with different concentrations of IR-FCD NPs and IR-FCD-Ts NPs without laser irradiation. Error bars, mean ± SD (n = 3). Fig. S19 Flow cytometric analysis of apoptosis levels in 4T1 cells after different treatments (+ L represents 1064 nm laser irradiation at 1.0 W/cm^2 for 10 min). Fig. S20 (A-E) The MFI data of Fig.3F-3J. Error bars: mean ± SD (n = 3). Fig. S21 (A-D) Western blot analysis was conducted to evaluate the expression levels of CHOP, Cleaved Caspase-3, CRT, and HMGB1 in 4T1 cells subjected to different treatments (I: PBS, II: PBS + L, III: IR-FCD NPs, IV: IR-FCD NPs + L, V: IR-FCD-Ts NPs, VI: IR-FCD-Ts NPs + L. + L represents 1064 nm laser irradiation at 1.0 W/cm^2 for 10 min). Fig. S22 Analysis of ATP levels in 4T1 cell culture supernatants after different treatments (I: PBS, II: PBS + L, III: IR-FCD NPs, IV: IR-FCD NPs + L, V: IR-FCD-Ts NPs, VI: IR-FCD-Ts NPs + L.+ L represents 1064 nm laser irradiation at 1.0 W/cm^2 for 10 min). Error bars, mean ± SD (n = 3). Fig. S23 Complete blood count and blood biochemical analysis of healthy mice on the 15th day after injection of nanoparticles and PBS. Error bars, mean ± SD (n = 3). Fig. S24 H&E staining images of major organs (heart, liver, spleen, lung, and kidney) after the injection with PBS and nanoparticles in healthy mice on day 15. Scale bar: 100 μm. Fig. S25 The tumor-to-normal tissue (T/N) ratio of NIR-II fluorescence imaging in 4T1 tumor-bearing mice was assessed at various time points following injection. Fig. S26 (A) Fluorescent imaging of primary organs and tumor tissues taken 48 h following injection. (B) Semi-quantitative biodistribution analysis was conducted based on the fluorescence intensities of tumors and major organs at 48 h. Error bars, mean ± SD (n = 3). Fig. S27 NIR-II fluorescence imaging of major organs and excretions in mice at different time points after injection of IR-FCD-Ts NPs. Fig. S28 Individual growth curves of the primary tumors in mice following different treatments (I: PBS, II: PBS + L, III: IR-FCD NPs, IV: IR-FCD NPs + L, V: IR-FCD-Ts NPs, VI: IR-FCD-Ts NPs + L. + L represents 1064 nm laser irradiation at 1.0 W/cm^2 for 10 min). Fig. S29 Individual growth curves of the distant tumors in mice following different treatments (I: PBS, II: PBS + L, III: IR-FCD NPs, IV: IR-FCD NPs + L, V: IR-FCD-Ts NPs, VI: IR-FCD-Ts NPs + L. + L represents 1064 nm laser irradiation at 1.0 W/cm^2 for 10 min). Fig. S30 H&E, Ki-67, TUNE staining images of the dissected primary tumor tissues after various treatments (I: PBS, II: PBS + L, III: IR-FCD NPs, IV: IR-FCD NPs + L, V: IR-FCD-Ts NPs, VI: IR-FCD-Ts NPs + L.+ L represents 1064 nm laser irradiation at 1.0 W/cm^2 for 10 min). Scale bar: 50 μm. Fig. S31 Quantification of lung metastatic nodules in different treatment groups (I: PBS, II: PBS + L, III: IR-FCD NPs, IV: IR-FCD NPs + L, V: IR-FCD-Ts NPs, VI: IR-FCD-Ts NPs + L. + L represents 1064 nm laser irradiation at 1.0 W/cm^2 for 10 min). Fig. S32 Representative immune fluorescence images staining images to show CD8$^+$ T cells and Tregs in tumors of different treated mice (I: PBS, II: PBS + L, III: IR-FCD NPs, IV: IR-FCD NPs + L, V: IR-FCD-Ts NPs, VI: IR-FCD-Ts NPs + L. + L represents 1064 nm laser irradiation at 1.0 W/cm^2 for 10 min). Scale bar: 50 μm. Fig. S33 The representative flow cytometric analyses of effector memory cells (CD44$^+$ CD62L$^-$) in CD8$^+$ T cells in distant tumors and spleens after different treatments (I: PBS, II: PBS + L, III: IR-FCD NPs, IV: IR-FCD NPs + L, V: IR-FCD-Ts NPs, VI: IR-FCD-Ts NPs + L. + L represents 1064 nm laser irradiation at 1.0 W/cm^2 for 10 min). Fig. S34 (A) Proportions of mature DCs (CD80$^+$ CD86$^+$ CD11C$^+$) in primary tumor tissues. (B) Proportions of CTLs (CD3$^+$ CD8$^+$) in primary tumor tissues. (C) Proportions of Tregs (CD4$^+$ CD25$^+$ Foxp3$^+$) in primary tumor tissues. Proportions of effector memory T cells (CD3$^+$ CD8$^+$ CD44$^+$ CD62L$^-$) in (D) distant tumors and (E) spleens. (I: PBS, II: PBS + L, III: IR-FCD NPs, IV: IR-FCD NPs + L, V: IR-FCD-Ts NPs, VI: IR-FCD-Ts NPs + L.+ L represents 1064 nm laser irradiation at 1.0 W/cm^2 for 10 min). Error bars: mean±SD (n = 3). Fig. S35 Representative immune fluorescence images staining images to show CD8$^+$ T cells in distant tumors and spleens after different treatments (I: PBS, II: PBS + L, III: IR-FCD NPs, IV: IR-FCD NPs + L, V: IR-FCD-Ts NPs, VI: IR-FCD-Ts NPs + L. + L represents 1064 nm laser irradiation at 1.0 W/cm^2 for 10 min). Scale bar: 50 μm. Table S1 LUMO composition analysis results of the molecular fluorophores IR-FTT IR-FCD based on the Hirshfeld method by Multiwfn. Table S2 Calculated first vertical S_0-S_1 excitation energies (E_{01}), first vertical S_1-S_0 emission energies (E_{10}), electronic configurations, and reorganization energies determined at the TD-ωB97XD*/6-31G (d) level of theory in vacuum.

Acknowledgements

Q.L.Y. acknowledges financial support from the National Science Foundation of China (22374065), the Outstanding Youth Foundation of Hunan Province (2024JJ2047), the Key Research and Development Program of Hunan Province, China (2022SK2053), and the Aid Program for Science and Technology Innovative Research Team in Higher Educational Institutions of Hunan Province. F.L. thanks the Natural Science Foundation of Hunan Province of China (2025JJ81013) and the Scientific Research Fund of Hunan Province Education Department (24B0393) for funding support. G.L.W. thanks the Natural Science Foundation of Hunan Province of China (2024JJ6374) and the Scientific Research Fund of Hunan Province Education Department (24B0427) for funding support. The authors would also like to thank Shiyanjia Lab (www.shiyanjia.com) for the support of the TEM tests.

Author contributions

Q.L.Y., X.F.T., and F.L. conceived and designed the experiments. F.L., Q.K., J.C.P., Y.Y.L., K.F, and S.Y.T performed the experiments. F.L., Q.K., and G.L.W. analyzed the data. F.L., X.F.T., and Q.L.Y. wrote the manuscript. All authors discussed the results and commented on the manuscript.

Funding

This work was supported by the National Science Foundation of China (22374065), the Outstanding Youth Foundation of Hunan Province (2024JJ2047), the Key Research and Development Program of Hunan Province, China (2022SK2053), the Aid Program for Science and Technology Innovative Research Team in Higher Educational Institutions of Hunan Province, the Natural Science Foundation of Hunan Province of China (2024JJ6374, 2025JJ81013) and the Scientific Research Fund of Hunan Province Education Department (24B0427, 24B0393).

Availability of data and materials

No datasets were generated or analysed during the current study.

Declarations

Consent for publication

All authors read and agreed to submit the manuscript.

Competing interests
The authors declare no competing interests.

Author details
[1]Department of Hepatopancreatobiliary Surgery, the First Affiliated Hospital & Center for Molecular Imaging Probe, Hengyang Medical School, Cancer Research Institute, University of South China, Hengyang 421001, Hunan, China. [2]Department of Radiology, The Second Affiliated Hospital, University of South China, Hengyang 421001, Hunan, China. [3]NHC Key Laboratory of Birth Defect Research and Prevention & MOE Key Lab of Rare Pediatric Disease & Hunan Engineering Research Center for Early Diagnosis and Treatment of Liver Cancer Hengyang Medical School, University of South China, Hengyang 421001, Hunan, China.

Received: 29 November 2024 Accepted: 26 February 2025
Published online: 22 March 2025

References

1. Leon-Ferre RA, Goetz MP. Advances in systemic therapies for triple negative breast cancer. BMJ. 2023;381: e071674.
2. Bianchini G, Balko JM, Mayer IA, Sanders ME, Gianni L. Triple-negative breast cancer: challenges and opportunities of a heterogeneous disease. Nat Rev Clin Oncol. 2016;13:674–90.
3. Obidiro O, Battogtokh G, Akala EO. Triple negative breast cancer treatment options and limitations: future outlook. Pharmaceutics. 2023;15:1796.
4. So JY, Ohm J, Lipkowitz S, Yang L. Triple negative breast cancer (TNBC): non-genetic tumor heterogeneity and immune microenvironment: emerging treatment options. Pharmacol Ther. 2022;237:108253.
5. Wang C, Sun Y, Huang S, Wei Z, Tan J, Wu C, Chen Q, Zhang X. Self-immolative photosensitizers for self-reported cancer phototheranostics. J Am Chem Soc. 2023;145:13099–113.
6. Long Y, Fan J, Zhou N, Liang J, Xiao C, Tong C, Wang W, Liu B. Biomimetic Prussian blue nanocomplexes for chemo-photothermal treatment of triple-negative breast cancer by enhancing ICD. Biomaterials. 2023;303:122369.
7. Zhang G, Chen X, Chen X, Du K, Ding K, He D, Ding D, Hu R, Qin A, Tang BZ. Click-reaction-mediated chemotherapy and photothermal therapy synergistically inhibit breast cancer in mice. ACS Nano. 2023;17:14800–13.
8. Pan Y, Cheng J, Zhu Y, Zhang J, Fan W, Chen X. Immunological nanomaterials to combat cancer metastasis. Chem Soc Rev. 2024;53:6399–444.
9. Ma X, Zhang MJ, Wang J, Zhang T, Xue P, Kang Y, Sun ZJ, Xu Z. Emerging biomaterials imaging antitumor immune response. Adv Mater. 2022;34: e2204034.
10. Feng Z, Tang T, Wu T, Yu X, Zhang Y, Wang M, Zheng J, Ying Y, Chen S, Zhou J, et al. Perfecting and extending the near-infrared imaging window. Light Sci Appl. 2021;10:197.
11. Zhang Z, Du Y, Shi X, Wang K, Qu Q, Liang Q, Ma X, He K, Chi C, Tang J, et al. NIR-II light in clinical oncology: opportunities and challenges. Nat Rev Clin Oncol. 2024;21:449–67.
12. He S, Song J, Qu J, Cheng Z. Crucial breakthrough of second near-infrared biological window fluorophores: design and synthesis toward multimodal imaging and theranostics. Chem Soc Rev. 2018;47:4258–78.
13. Yang S, Li N, Xiao H, Wu GL, Liu F, Qi P, Tang L, Tan X, Yang Q. Clearance pathways of near-infrared-II contrast agents. Theranostics. 2022;12:7853–83.
14. Zhang J, Wang W, Shao J, Chen J, Dong X. Small molecular cyanine dyes for phototheranostics. Coord Chem Rev. 2024;516:215986.
15. Meador WE, Lin EY, Lim I, Friedman HC, Ndaleh D, Shaik AK, Hammer NI, Yang B, Caram JR, Sletten EM, Delcamp JH. Silicon-RosIndolizine fluorophores with shortwave infrared absorption and emission profiles enable in vivo fluorescence imaging. Nat Chem. 2024;16:970–8.
16. Liu S, Li Y, Kwok RTK, Lam JWY, Tang BZ. Structural and process controls of AIEgens for NIR-II theranostics. Chem Sci. 2020;12:3427–36.
17. Shao W, Wei Q, Wang S, Li F, Wu J, Ren J, Cao F, Liao H, Gao J, Zhou M, Ling D. Molecular engineering of D–A–D conjugated small molecule nanoparticles for high performance NIR-II photothermal therapy. Mater Horiz. 2020;7:1379–86.
18. Bandi VG, Luciano MP, Saccomano M, Patel NL, Bischof TS, Lingg JGP, Tsrunchev PT, Nix MN, Ruehle B, Sanders C, et al. Targeted multicolor in vivo imaging over 1000 nm enabled by nonamethine cyanines. Nat Methods. 2022;19:353–8.
19. Mao Z, Kim JH, Lee J, Xiong H, Zhang F, Kim JS. Engineering of BODIPY-based theranostics for cancer therapy. Coord Chem Rev. 2023;476:214908.
20. Shao W, Zhao F, Xue J, Huang L. NIR-II absorbing organic nanoagents for photoacoustic imaging and photothermal therapy. BMEMat. 2023;1: e12009.
21. Jiang Z, Zhang C, Wang X, Yan M, Ling Z, Chen Y, Liu Z. A borondifluoride-complex-based photothermal agent with an 80 % photothermal conversion efficiency for photothermal therapy in the NIR-II window. Angew Chem Int Ed. 2021;60:22376–84.
22. Wang X, Qian J, Yang Z, Song Y, Pan W, Ye Y, Qin X, Yan X, Huang X, Wang X, et al. Photodynamic modulation of endoplasmic reticulum and mitochondria network boosted cancer immunotherapy. Adv Mater. 2024;36: e2310964.
23. Li Z, Zou J, Chen X. In response to precision medicine: current subcellular targeting strategies for cancer therapy. Adv Mater. 2023;35: e2209529.
24. Chen P, Qu F, Chen S, Li J, Shen Q, Sun P, Fan Q. Bandgap modulation and lipid intercalation generates ultrabright D–A–D-based zwitterionic small-molecule nanoagent for precise NIR-II excitation phototheranostic applications. Adv Funct Mater. 2022;32:2208463.
25. Song S, Zhao Y, Kang M, Zhang F, Wu Q, Niu N, Yang H, Wen H, Fu S, Li X, et al. An NIR-II excitable AIE small molecule with multimodal phototheranostic features for orthotopic breast cancer treatment. Adv Mater. 2024;36: e2309748.
26. Yan D, Zhang Z, Zhang J, Li X, Wu Q, Gui Y, Zhu J, Kang M, Chen X, Tang BZ, Wang D. An all-rounder for NIR-II phototheranostics: well-tailored 1064 nm-excitable molecule for photothermal combating of orthotopic breast cancer. Angew Chem Int Ed. 2024;63: e202401877.
27. Yang Q, Hu Z, Zhu S, Ma R, Ma H, Ma Z, Wan H, Zhu T, Jiang Z, Liu W, et al. Donor engineering for NIR-II molecular fluorophores with enhanced fluorescent performance. J Am Chem Soc. 2018;140:1715–24.
28. Wang R, Li X, Yoon J. Organelle-targeted photosensitizers for precision photodynamic therapy. ACS Appl Mater. 2021;13:19543–71.
29. Wen Y, Schreiber CL, Smith BD. Dual-targeted phototherapeutic agents as magic bullets for cancer. Bioconjug Chem. 2020;31:474–82.
30. Chen X, Cubillos-Ruiz JR. Endoplasmic reticulum stress signals in the tumour and its microenvironment. Nat Rev Cancer. 2021;21:71–88.
31. Ma H, Lu Y, Huang Z, Long S, Cao J, Zhang Z, Zhou X, Shi C, Sun W, Du J. ER-targeting cyanine dye as an NIR photoinducer to efficiently trigger photoimmunogenic cancer cell death. J Am Chem Soc. 2022;144:3477–86.
32. Liu X, Liu Y, Li X, Huang J, Guo X, Zhang J, Luo Z, Shi Y, Jiang M, Qin B, et al. ER-targeting PDT converts tumors into in situ therapeutic tumor vaccines. ACS Nano. 2022;16:9240–53.
33. Huang X, Gao M, Xing H, Du Z, Wu Z, Liu J, Li T, Cao J, Yang X, Li R, et al. Rationally designed heptamethine cyanine photosensitizers that amplify tumor-specific endoplasmic reticulum stress and boost antitumor immunity. Small. 2022;18: e2202728.
34. Zhang X, Wan J, Mo F, Tang D, Xiao H, Li Z, Jia J, Liu T. Targeting bone tumor and subcellular endoplasmic reticulum via near infrared II fluorescent polymer for photodynamic-immunotherapy to break the step-reduction delivery dilemma. Adv Sci. 2022;9: e2201819.
35. Deng H, Zhou Z, Yang W, Lin LS, Wang S, Niu G, Song J, Chen X. Endoplasmic reticulum targeting to amplify immunogenic cell death for cancer immunotherapy. Nano Lett. 2020;20:1928–33.
36. Yang Q, Ma Z, Wang H, Zhou B, Zhu S, Zhong Y, Wang J, Wan H, Antaris A, Ma R, et al. Rational design of molecular fluorophores for biological imaging in the NIR-II window. Adv Mater. 2017;29:1605497.
37. Cao W, Zhang X, Yang X, Sun H, Chen Z, Liang Y. Quinoidal π-bridges for a fused-ring acceptor with enhanced near-infrared-II photothermal therapy and fluorescent emission beyond 1500 nm. ACS Mater Lett. 2024;6:2687–95.
38. Pan Q, Li K, Kang X, Li K, Cheng Z, Wang Y, Xu Y, Li L, Li N, Wu G, et al. Rational design of NIR-II molecule-engineered nanoplatform for preoperative downstaging and imaging-guided surgery of orthotopic hepatic tumor. J Nanobiotechnol. 2023;21:489.

39. Wu GL, Liu F, Li N, Fu Q, Wang CK, Yang S, Xiao H, Tang L, Wang F, Zhou W, et al. Trisulfide bond-mediated molecular phototheranostic platform for "activatable" NIR-II imaging-guided enhanced gas/chemo-hypothermal photothermal therapy. Adv Sci. 2023;10: e2304104.
40. Ma H, Liu C, Hu Z, Yu P, Zhu X, Ma R, Sun Z, Zhang C-H, Sun H, Zhu S, Liang Y. Propylenedioxy thiophene donor to achieve NIR-II molecular fluorophores with enhanced brightness. Chem Mater. 2020;32:2061–9.
41. Liu C, Li M, Ma H, Hu Z, Wang X, Ma R, Jiang Y, Sun H, Zhu S, Liang Y. Furan donor for NIR-II molecular fluorophores with enhanced bioimaging performance. Research. 2023;6:0039.
42. Yang Q, Ma H, Liang Y, Dai H. Rational design of high brightness NIR-II organic dyes with S-D-A-D-S structure. Acc Mater Res. 2021;2:170–83.
43. Li Z, Yang S, Xiao H, Kang Q, Li N, Wu G-l, Tan S, Wang W, Fu Q, Tang X, et al. Lysosome-targeted and pH-activatable phototheranostics for NIR-II fluorescence imaging-guided nasopharyngeal carcinoma phototherapy. Bioconj Chem. 2024;35:1015–23.
44. Yang S, Sun B, Liu F, Li N, Wang M, Wu P, Wu GL, Fang H, He Y, Zhou W, et al. NIR-II imaging-guided mitochondrial-targeting organic nanoparticles for multimodal synergistic tumor therapy. Small. 2023;19: e2207995.
45. Sun B, Ma R, Wang X, Ma S, Li W, Liu T, Zhu W, Ji Z, Hettie KS, Liu C, Liang Y, Zhu S. A high-performance cell-labeling NIR-II dye for in vivo cell tracking. VIEW. 2024;5:20230097.
46. Gu Y, Lai H, Chen ZY, Zhu Y, Sun Z, Lai X, Wang H, Wei Z, Chen L, Huang L. Chlorination-mediated π–π stacking enhances the photodynamic properties of a NIR-II emitting photosensitizer with extended conjugation. Angew Chem Int Ed. 2023;135: e202303476.
47. Shen Y, Zhang Z, Liu H, Yan Y, Zhang S, Yang B, Ma Y. Highly efficient orange-red/red excimer fluorescence from dimeric π–π stacking of perylene and its nanoparticle applications. J Phys Chem C. 2019;123:13047–56.
48. Xiong Y, Li J, He S. Zinc Protects against heat stress-induced apoptosis via the inhibition of endoplasmic reticulum stress in TM3 Leydig cells. Biol Trace Elem Res. 2022;200:728–39.
49. Feng X, Lin T, Chen D, Li Z, Yang Q, Tian H, Xiao Y, Lin M, Liang M, Guo W, et al. Mitochondria-associated ER stress evokes immunogenic cell death through the ROS-PERK-eIF2alpha pathway under PTT/CDT combined therapy. Acta Biomater. 2023;160:211–24.
50. Xu L, Zhang X, Tian Y, Fan Z, Li W, Liu M, Hu J, Duan Z, Jin R, Ren F. The critical role of PPARalpha in the binary switch between life and death induced by endoplasmic reticulum stress. Cell Death Dis. 2020;11:691.
51. Ngo W, Ahmed S, Blackadar C, Bussin B, Ji Q, Mladjenovic SM, Sepahi Z, Chan WCW. Why nanoparticles prefer liver macrophage cell uptake in vivo. Adv Drug Deliv Rev. 2022;185:114238.
52. Chen YY, Syed AM, MacMillan P, Rocheleau JV, Chan WCW. Flow rate affects nanoparticle uptake into endothelial cells. Adv Mater. 2020;32: e1906274.
53. Pu Y, He L, Wang X, Zhang Y, Zhao S, Fan J. Global, regional, and national levels and trends in burden of urticaria: a systematic analysis for the Global Burden of Disease study 2019. J Glob Health. 2024;14:04095.

Publisher's Note